

# An investigation into the power spectrums of matter and radiation

Johan Mylius Kroken<sup>1,2</sup>

<sup>1</sup> Institute of Theoretical Astrophysics (ITA), University of Oslo, Norway

<sup>2</sup> Center for Computing in Science Education (CCSE), University of Oslo, Norway

June 1, 2023 - GitHub repository link: <https://github.com/Johanmkr/AST5220/tree/main/project>

## ABSTRACT

The cosmic microwave background radiation can be seen across the entire sky, and can provide great insight into the nature of several cosmological phenomena. It is therefore of interest to investigate this theoretically, which is the main aim of this article. We consider linear perturbation to the FLRW cosmology in conformal Newtonian gauge in order to create a pipeline for predicting the power spectra of matter and anisotropies to the CMB. This is done by first calculating the background cosmology, and recombination epoch, including neutrinos. We then ignore neutrinos, polarisation and reionisation when evolving the perturbation equations in time, in order to solve for the power spectra which can be compared with observations. Ignoring these effects yield a significant discrepancy in the result for small scale modes, but provide enough accuracy for the large scale modes. As a result, we obtain a pipeline through which we can obtain power spectra for different cosmologies and compare them to data, although the analysis is only done for the  $\Lambda$ CDM-cosmology using data from [Aghanim et al. \(2020\)](#).

## Contents

<b>1</b>	<b>Introduction</b>	<b>3</b>	4.1.6	Tight coupling regime	16
<b>2</b>	<b>Background Cosmology</b>	<b>3</b>	4.1.7	Modes, scales and the horizon	17
2.1	Theory	3	4.1.8	Inflation	17
2.1.1	Fundamentals	3	4.1.9	Initial conditions	18
2.1.2	Measure of time and space	4	4.1.10	Line of sight integration	19
2.1.3	$\Lambda$ CDM-model	5	4.1.11	Analytical expectations	20
2.1.4	Analytical solutions and sanity checks	5	4.2	Methods	20
2.2	Methods	6	4.3	Results and discussion	20
2.2.1	ODEs and Splines	6	4.3.1	Potentials	21
2.2.2	Fit to supernova data	6	4.3.2	Multipoles	21
2.3	Results and discussion	7	4.3.3	Matter perturbations	22
2.3.1	Tests	7	<b>5</b>	<b>Power spectrums</b>	<b>23</b>
2.3.2	Analysis	7	5.1	Theory	23
<b>3</b>	<b>Recombination History</b>	<b>9</b>	5.1.1	Physical observables	24
3.1	Theory	10	5.1.2	Constructing the angular power spectrum	25
3.1.1	Hydrogen recombination	10	5.1.3	Matter power spectrum	25
3.1.2	Visibility	11	5.2	Methods	26
3.1.3	Sound horizon	11	5.2.1	Making Bessel splines	26
3.2	Methods	11	5.2.2	Line of sight integration	26
3.2.1	Computing $X_e$	11	5.2.3	Integrate across $k$	26
3.2.2	Computing $\tau$ and $\tilde{g}$	12	5.2.4	Numerical integration	27
3.2.3	Analysis	12	5.3	Results and discussion	27
3.3	Results and discussion	12	5.3.1	The Sachs-Wolfe plateau	27
3.3.1	Times and sound horizon	12	5.3.2	Acoustic oscillations	28
3.3.2	Free electron fraction	12	5.3.3	The damping tail	28
3.3.3	Visibility	13	5.3.4	Parameter dependence	28
3.3.4	General discussion	13	5.3.5	The matter power spectrum	29
<b>4</b>	<b>Perturbations</b>	<b>13</b>	<b>6</b>	<b>Conclusion</b>	<b>30</b>
4.1	Theory	14			
4.1.1	Metric perturbations	14			
4.1.2	Fourier space and multipole expansion	14			
4.1.3	Photon perturbation	15			
4.1.4	Matter perturbation	15			
4.1.5	Evolutionary equations	15			

## Nomenclature

### Constants of nature

- $m_e$  - Mass of electron.  
 $m_e = 9.10938356 \cdot 10^{-31}$  kg.  
 $m_H$  - Mass of hydrogen atom.  
 $m_H = 1.6735575 \cdot 10^{-27}$  kg.  
 $G$  - Gravitational constant.  
 $G = 6.67430 \cdot 10^{-11}$  m<sup>3</sup> kg<sup>-1</sup> s<sup>-2</sup>.  
 $k_B$  - Boltzmann constant.  
 $k_B = 1.38064852 \cdot 10^{-23}$  m<sup>2</sup> kg s<sup>-2</sup> K<sup>-1</sup>.  
 $\hbar$  - Reduced Planck constant.  
 $\hbar = 1.054571817 \cdot 10^{-34}$  J s<sup>-1</sup>.  
 $c$  - Speed of light in vacuum.  
 $c = 2.99792458 \cdot 10^8$  m s<sup>-1</sup>.  
 $\sigma_T$  - Thomson cross section.  
 $\sigma_T = 6.6524587158 \cdot 10^{-29}$  m<sup>2</sup>.  
 $\alpha$  - Fine structure constant.  
 $\alpha = \frac{m_e c}{\hbar} \sqrt{\frac{3\sigma_T}{8\pi}}$

### Cosmological parameters

- $G_{\mu\nu}$  - Einstein tensor.  
 $T_{\mu\nu}$  - Stress-energy tensor.  
 $H$  - Hubble parameter.  
 $\mathcal{H}$  - Conformal Hubble parameter.  
 $T_{\text{CMB0}}$  - Temperature of CMB today.  
 $a$  - Scale factor.  
 $x$  - Logarithm of scale factor.  
 $t$  - Cosmic time.  
 $z$  - Redshift.  
 $\eta$  - Conformal time.  
 $\chi$  - Co-moving distance.  
 $p$  - Pressure.  
 $\rho$  - Density.  
 $r$  - Radial distance.  
 $d_A$  - Angular diameter distance.  
 $d_L$  - Luminosity distance.  


---

 $n_e$  - Electron density.  
 $n_b$  - Baryon density.  
 $X_e$  - Free electron fraction.  
 $\tau$  - Optical depth.  
 $\tilde{g}$  - Visibility function.  
 $s$  - Sound horizon.  
 $r_s$  - Sound horizon at decoupling.  
 $c_s$  - Wave propagation speed.  


---

 $\Psi$  - Newtonian potential perturbation to the metric.  
 $\Phi$  - Spatial curvature perturbation to the metric.  
 $P^\mu$  - Comoving momentum four vector.  
 $\mathcal{P}_l$  - Legendre polynomial of order  $l$ .  
 $k$  - Fourier mode  $k = \mathbf{k}$  of wave vector  $\mathbf{k}$ .  
 $\Theta$  - Photon perturbation.  
 $\Theta_l$  -  $l$ -th order multipole expansion term of  $\Theta$ .  
 $v_b$  - Baryon bulk velocity.  
 $v_c$  - Cold dark matter bulk velocity.  
 $v_\gamma$  - Photon bulk velocity.  
 $\delta_b$  - Baryon overdensity.  
 $\delta_c$  - Cold dark matter overdensity.  
 $\delta_\gamma$  - Photon overdensity.  
 $\phi$  - Inflaton field.  
 $\rho_\phi$  - Inflaton field density.  
 $p_\phi$  - Inflaton field pressure.

- $\epsilon_{\text{sr}}, \delta_{\text{sr}}$  - Slow roll parameters.  
 $\mathcal{R}$  - Curvature perturbation.  
 $S$  - Source function.

- $\Theta^{\text{Obs}}$  - Observed temperature anisotropies.  
 $Y_{lm}$  - Spherical harmonic functions.  
 $a_{lm}$  - Coefficients in spherical harmonic expansion.  
 $C_l$  - Angular power spectrum.  
 $P_{\text{prim}}$  - Primordial power spectrum.  
 $n_s$  - Spectral index.  
 $A_s$  - Primordial amplitude.  
 $\Delta_M$  - Total matter contrast.  
 $P$  - Matter power spectrum.  
 $j_l$  - Spherical Bessel function.

### Density parameters

Density parameter  $\Omega_X = \rho_X / \rho_{\text{crit}}$  where  $\rho_X$  is the density and  $\rho_c = 8\pi G / 3H^2$  the critical density.  $X$  can take the following values:

- $b$  - Baryons.  
 $c$  - Cold dark matter.  
 $\gamma$  - Electromagnetic radiation.  
 $\nu$  - Neutrinos.  
 $k$  - Spatial curvature.  
 $\Lambda$  - Cosmological constant.

A 0 in the subscript indicates the present day value.

### Fiducial cosmology

The fiducial cosmology used throughout this project is based on the observational data obtained by [Aghanim et al. \(2020\)](#):

$$\begin{aligned}
 h &= 0.67, \\
 T_{\text{CMB0}} &= 2.7255 \text{ K}, \\
 N_{\text{eff}} &= 3.046, \\
 \Omega_{b0} &= 0.05, \\
 \Omega_{c0} &= 0.267, \\
 \Omega_{k0} &= 0, \\
 \Omega_{\nu0} &= N_{\text{eff}} \cdot \frac{7}{8} \left( \frac{4}{11} \right)^{4/3} \Omega_{\gamma0}, \\
 \Omega_{\Lambda0} &= 1 - (\Omega_{k0} + \Omega_{b0} + \Omega_{\text{CDM0}} + \Omega_{\gamma0} + \Omega_{\nu0}), \\
 \Omega_{M0} &= \Omega_{b0} + \Omega_{\text{CDM0}}, \\
 \Omega_{\text{rad}} &= \Omega_{\gamma0} + \Omega_{\nu0}, \\
 n_s &= 0.965, \\
 A_s &= 2.1 \cdot 10^{-9}.
 \end{aligned}$$

## 1. Introduction

The Cosmic Microwave Background radiation is the leftover radiation from the early universe. It is the most ancient light we can observe, having travelled towards us ever since the Universe became transparent. Therefore, it contains a significant amount of information so understanding its nature is of utmost importance for us. We observe small fluctuations in the CMB across the entire sky. Hence, one main question we will try to answer is: Why are there fluctuations in the CMB?

In this project we take a closer look at the CMB power spectrum. This is a plot that shows the distribution of temperature fluctuations in the CMB across different angular scalar. This is of great significance to us, since the CMB power spectrum is able to reveal information about the cosmological parameters of our universe, such as the various density components and Hubble constant. It is also able to tell us something about the large scale structures of the Universe, and the overall geometry of space itself. Also, which is perhaps the most interesting, it can yield information about the nature of dark energy.

The overarching aim is to produce a pipeline that allows us to calculate numerically the CMB power spectrum and matter power spectrum given some cosmological model. The steps will be presented chronologically, and we start by setting up the background cosmology in Section 2. Here we solve the evolutionary equations for an isotropic and homogeneous universe using the  $\Lambda$ CDM-model. One particularly important event in the evolution of the CMB is recombination, ultimately leading to photon decoupling. After this, the photons free stream towards us which is what we today see as the CMB. The entire Section 3 is devoted to this event, and the time right before and right after it. In Section 4 we take a step away from the isotropic and homogeneous universe and consider perturbations to the metric in conformal Newtonian gauge. The implications these metric perturbations have on the distribution of matter is discussed, and we end up with a set of coupled differential equations that we can solve numerically. The initial conditions of these are found by considering the period of inflation in the very early Universe. We learn to evolve all the perturbation, given some initial conditions, until today. Section 5 concerns itself with finding the initial conditions in order to compare the computed values with actual observables. This is done by constructing power spectrums; the angular power spectrum of the CMB and the matter power spectrum of the total density contrast. This comparison allow us to theoretically constrain the model parameter.

We will only consider neutrinos when we solve the background cosmology and recombination epoch. For the rest of the project, neutrinos are ignored. Polarisation and the epoch of reionisation are ignored throughout. We also ignore the relatively small abundance of especially helium, but also heavier elements.

## 2. Background Cosmology

According to the cosmological principle, the universe is homogeneous and isotropic on a large scale. Hence, there are no preferred locations nor directions. Furthermore, we may safely assume that the physical laws that govern our local part of the universe is equally valid elsewhere.

The aim now is to set up the background cosmology, in which the investigation of all interesting phenomena will take place. Setting up the background cosmology is practically equivalent to solving the *Einstein field equation*:

$$G_{\mu\nu} = 8\pi G T_{\mu\nu}, \quad (1)$$

where  $G_{\mu\nu}$  is the Einstein tensor describing the geometry of spacetime,  $G$  is the gravitational constant and  $T_{\mu\nu}$  is the energy and momentum tensor. This equation relates the geometry and shape of spacetime itself, to its energy content (matter included). There are many solutions to Eq. (1), but we want the solution to govern a universe that is spatially isotropic and homogeneous, but may evolve in time. The spacetime metric that satisfies this conditions is the *Friedmann-Lemaître-Robertson-Walker metric* (FLRW) (Carroll 2019, ch. 8).

We will use this metric in order to describe the background universe, how it may evolve in time, and its history.

### 2.1. Theory

When considering the theory of the background cosmology we will first find the evolutionary equations of space itself from Eq. (1). Next we investigate the concepts of space and time and how we can measure them, before we finally delve into the cosmological model we will use: The  $\Lambda$ CDM-model. We evolve the density parameters of this model in time. Lastly, we put constraints on them through comparison with observational data from supernovas.

#### 2.1.1. Fundamentals

If we assume the universe to be homogeneous and isotropic, the line elements  $ds$  is given by the FLRW-metric, here in polar coordinates (Weinberg 2008, eq. 1.1.11):

$$ds^2 = -dt^2 + e^{2x} \left[ \frac{dr^2}{1 - kr^2} + r^2 d\theta^2 + r^2 \sin^2 \theta d\phi^2 \right], \quad (2)$$

where we have introduced  $x = \ln(a)$  which will be our primary measure of time, which will be explained later.

We further model all forms of energy in the universe as perfect fluids, only characterised by their rest frame density  $\rho$  and isotropic pressure  $p$ , and an equation of state relating the two:

$$\omega = \frac{p}{\rho}. \quad (3)$$

By conservation of energy and momentum we must satisfy  $\nabla_\mu T^{\mu\nu} = 0$ , which results in the following differential equations for the density of each fluid  $\rho_i$ , from Winther et al. (2023):

$$\frac{d\rho_i}{dt} + 3H\rho_i(1 + \omega_i) = 0, \quad (4)$$

where we have introduced the Hubble parameter  $H \equiv \dot{a}/a = dx/dt$ . The solution to Eq. (4) is of the form:

$$\rho_i \propto e^{-3(1+\omega_i)x}, \quad (5)$$

where  $\omega_M = 0$  (matter),  $\omega_{\text{rad}} = 1/3$  (radiation),  $\omega_\Lambda = -1$  (cosmological constant) and  $\omega_k = -1/3$  (curvature).

With these assumptions, the solution to the Einstein equations, Eq. (1) are the Friedmann equations (Carroll 2019, ch. 8.3), the first of which describes the expansion rate of the universe:

$$H^2 = \frac{8\pi G}{3} \sum_i \rho_i - kc^2 e^{-2x} \quad (6)$$

and the second describe how this expansion rate changes over time:

$$\frac{dH}{dt} + H^2 = -\frac{4\pi G}{3} \sum_i \left( \rho_i + \frac{3p_i}{c^2} \right). \quad (7)$$

As of now, we are primarily interested in the first Friedmann equation. By introducing the critical density,  $\rho_{\text{crit}} \equiv 3H^2/(8\pi G)$ , we define the density parameters  $\Omega_i = \rho_i/\rho_{\text{crit}}$ . We further define the density  $\rho_k \equiv -3kc^2e^{-2x}/(8\pi G)$ ,<sup>1</sup> which enables us to write Eq. (6) as simply:

$$1 = \sum_i \Omega_i, \quad (8)$$

where the density  $\Omega_k$  is included in the sum. From Eq. (5) we know the evolution of the densities in time, and if we assume the density values today,  $\Omega_{i0}$ , are known (or are free parameters), then Eq. (6) may also be written as:

$$H = H_0 \sqrt{\sum_i \Omega_{i0} e^{-3(1+\omega_i)x}}, \quad (9)$$

which is the Hubble equation we will use further.

### 2.1.2. Measure of time and space

There are many ways of measuring time in cosmology, and they are often related to spatial quantities. The most common is perhaps the *scale factor*  $a$ , which describes how the physical size of the universe changes with time. An increasing scale factor signifies an expanding universe and vice versa. Another, computationally more useful way of describing  $a$  is through its logarithm  $x = \ln a \iff a = e^x$ , which is our convention of choice.

Another way of measuring the expansion of the Universe is through the *redshift*  $z$ , which is defined as the change in wavelength of electromagnetic radiation between emitter and observer. Radiation propagates through the Universe, so any expansion (or contraction) would expand (or contract) the wavelength, and this is encapsulated in the redshift  $z = \Delta\lambda/\lambda$ . It is connected to the scale factor as  $1 + z = 1/a$ .

Another, perhaps more familiar, time measure is the *cosmic time*  $t$ . This is the time<sup>2</sup> measured by a stationary observer (relative to the expanding universe). The statement: *The Universe is somewhat 13 billion years old*, is given in cosmic time, i.e. the time we experience on Earth.

Lastly, there is the *conformal time*  $\eta$ , defined as  $d\eta = cdte^{-x}$ .<sup>3</sup> This is a measure of distance (or rather the time it would take a light ray to traverse said distance) between points in space, where the expansion of space in between the points is taken into account. We use it to define the *particle horizon*, which is the horizon generated by the maximal conformal time elapsed since the Big Bang. This is how “far away” from the Big Bang any light ray could have propagated (expansion of the Universe included). This horizon expands with time, as we would expect, and this is what we mean by conformal time from now on; the extent of the particle horizon, beyond which there cannot be any causal connection. Hence, this is effectively the size of the causally connected universe.

Let’s express this mathematically, starting with the cosmic time:

$$t = \int_0^a \frac{da}{aH} = \int_{-\infty}^x \frac{dx}{H}. \quad (10)$$

<sup>1</sup> This is the “density of curvature”, but is in fact not a real density. It is called this because its mathematical behaviour is similar to that of the other (real) densities.

<sup>2</sup> In seconds, months, years, or any other preferred temporal unit (like the duration of a football match  $\pm$  added time).

<sup>3</sup> The  $c$  is sometimes omitted.  $d\eta = dte^{-x}$  has units of s, but multiplied with  $c$  yields the distance traversed by a light ray in this time; which is the particle horizon.

Using the definition of conformal time, we have:

$$\eta = \int_0^a \frac{cda}{a^2H} = \int_{-\infty}^x \frac{cdx}{e^xH} \equiv \int_{-\infty}^x \frac{cdx}{\mathcal{H}}, \quad (11)$$

where  $\mathcal{H} = e^xH$  is defined as the *conformal Hubble parameter*. We may then define the *comoving distance*,  $\chi$ , as the distance to a point, where we take the expansion of space into account, such that it becomes constant (given no relative motion). In contrast, while the proper distance between two points increase as the universe increase, the comoving distance remain constant. It is related to the conformal time, and given by:

$$\chi = \int_1^a \frac{cda}{a^2H} = \int_0^x \frac{cdx}{\mathcal{H}} = \eta_0 - \eta, \quad (12)$$

where  $\eta_0$  is the conformal time today. The radial coordinate in the FLRW line element, Eq. (2), is given in terms of the comoving distance and the curvature today  $\Omega_{k0}$  as:

$$r = \begin{cases} \chi \cdot \frac{\sin(\sqrt{|\Omega_{k0}|}H_0\chi/c)}{\sqrt{|\Omega_{k0}|}H_0\chi/c} & \Omega_{k0} < 0 \\ \chi & \Omega_{k0} = 0 \\ \chi \cdot \frac{\sinh(\sqrt{|\Omega_{k0}|}H_0\chi/c)}{\sqrt{|\Omega_{k0}|}H_0\chi/c} & \Omega_{k0} > 0 \end{cases} \quad (13)$$

Eq. (13) states that for an open universe ( $\Omega_{k0}$ ), radial coordinates evolves as a hyperbola, meaning photons take hyperbolic paths through spacetime. On the other hand, in a closed universe photons follow parabolic trajectories. From this, it is then straightforward to define the angular diameter distance:

$$d_A = e^x r, \quad (14)$$

and the luminosity distance:

$$d_L = e^{-x} r. \quad (15)$$

The temporal quantities  $\eta$  and  $t$  have the following evolutions with  $x$ :

$$\frac{d\eta}{dx} = \frac{c}{\mathcal{H}}. \quad (16)$$

$$\frac{dt}{dx} = \frac{1}{H}. \quad (17)$$

Both differential equations are easy to solve numerically.

### 2.1.3. $\Lambda$ CDM-model

In the  $\Lambda$ CDM model, the universe consists of matter in terms of baryonic matter ( $b$ ) and cold dark matter ( $c$ ), radiation in terms of photons ( $\gamma$ ) and neutrinos ( $\nu$ ) and dark energy in terms of a cosmological constant ( $\Lambda$ ). In addition, we must allow for some curvature ( $k$ ). As a result, the parameters of the model will be the present values of the Hubble rate,  $H_0$ , the baryon density  $\Omega_{b0}$ , the cold dark matter density  $\Omega_{c0}$ , photon density  $\Omega_{\gamma0}$ , neutrino density  $\Omega_{\nu0}$ , dark energy density  $\Omega_{\Lambda0}$ , and the curvature density  $\Omega_{k0}$ . The present temperature of the cosmic microwave background radiation  $T_{\text{CMB}0}$  fixes the radiation density today through:

$$\begin{aligned}\Omega_{\gamma0} &= \frac{16\pi^3 G}{90} \cdot \frac{(k_B T_{\text{CMB}0})^4}{\hbar^3 c^5 H_0^2}, \\ \Omega_{\nu0} &= N_{\text{eff}} \cdot \frac{7}{8} \cdot \left(\frac{4}{3}\right)^{4/3} \cdot \Omega_{\gamma0}.\end{aligned}\quad (18)$$

The total radiation density is  $\Omega_{\text{rad}} = \Omega_{\gamma} + \Omega_{\nu}$  and the total matter density is  $\Omega_{\text{M}} = \Omega_b + \Omega_c$ .

The Hubble equation from Eq. (9) may be redefined in terms of the conformal Hubble parameter  $\mathcal{H}$  as:

$$\begin{aligned}\mathcal{H} &= H_0 \sqrt{U} \\ U &\equiv \sum_i \Omega_{i0} e^{-\alpha_i x},\end{aligned}\quad (19)$$

where we have defined  $\alpha_i \equiv (1 + 3\omega_i)$  and  $i \in \{\text{M}, \text{rad}, \Lambda, k\}$ . Since we know the values of the various  $\omega_i$  it follows that:

$$\begin{aligned}\alpha_{\text{M}} &= 1 \\ \alpha_{\text{rad}} &= 2 \\ \alpha_k &= 0 \\ \alpha_{\Lambda} &= -2\end{aligned}\quad (20)$$

Given the evolution of the density parameters with time, where the proportionality constant is the present day density, we introduce the *radiation-matter equality*, i.e. the time radiation and matter densities were equal:  $\rho_{\text{rad}} = \rho_{\text{M}}$ . According to Eq. (5) this can be expressed as:

$$\begin{aligned}\rho_{\text{rad}0} e^{-4x} &= \rho_{\text{M}0} e^{-3x} \\ e^x &= \frac{\rho_{\text{rad}0}}{\rho_{\text{M}0}} \implies x_{\text{RM}} = \ln\left(\frac{\Omega_{\text{rad}0}}{\Omega_{\text{M}0}}\right),\end{aligned}\quad (21)$$

where  $x_{\text{RM}}$  now denotes the time of radiation-matter equality.

Similarly, the *matter-dark energy equality*, where  $\rho_{\text{M}} = \rho_{\Lambda}$  can be found to be:

$$\begin{aligned}\rho_{\Lambda} &= \rho_{\text{M}0} e^{-3x} \\ \implies x_{\text{M}\Lambda} &= \frac{1}{3} \ln\left(\frac{\Omega_{\text{M}0}}{\Omega_{\Lambda}}\right).\end{aligned}\quad (22)$$

Since  $\mathcal{H}$  describes the expansion of the Universe, it is fair to say that the acceleration of the Universe is governed by its second derivative, and the acceleration onset may be found from the extremal point in its first derivative. This means that we find the acceleration onset when:

$$\frac{d\mathcal{H}}{dx} = 0 \iff \frac{dU}{dx} = 0. \quad (23)$$

This follows from Eq. (19). We assume dark energy is involved in the acceleration of the universe, and thus assume the contribution from radiation is negligible. Eq. (23) is thus further reduced to:

$$\begin{aligned}2\Omega_{\Lambda0} e^{2x} - \Omega_{\text{M}0} e^{-x} &= 0 \\ \implies x_{\text{accel}} &= \frac{1}{3} \ln\left(\frac{\Omega_{\text{M}0}}{2\Omega_{\Lambda0}}\right).\end{aligned}\quad (24)$$

The age of the universe today, and the conformal time today can both be found by evaluating the solutions to the differential equations of  $t$  and  $\eta$  at the present time (where  $x = 0$ ). This is done numerically.

### 2.1.4. Analytical solutions and sanity checks

There are several ways we may check that both our workings and numerical implementations are indeed correct. The simplest way is to always ensure that the sum of all density parameters add up to 1, for all times:  $\sum_i \Omega_i = 1$ .

If we only consider the most dominant density parameter, that is  $\Omega_i \gg \sum_{j \neq i} \Omega_j$ , we end up with the following analytical expressions for different temporal regimes:

$$\frac{1}{\mathcal{H}} \frac{d\mathcal{H}}{dx} \approx -\frac{\alpha_i}{2} = \begin{cases} -1 & \alpha_{\text{rad}} = 2 \\ -\frac{1}{2} & \alpha_{\text{M}} = 1 \\ 1 & \alpha_{\Lambda} = -2 \end{cases} \quad (25)$$

$$\frac{1}{\mathcal{H}} \frac{d^2\mathcal{H}}{dx^2} \approx \frac{\alpha_i^2}{4} = \begin{cases} 1 & \alpha_{\text{rad}} = 2 \\ \frac{1}{4} & \alpha_{\text{M}} = 1 \\ 1 & \alpha_{\Lambda} = -2 \end{cases} \quad (26)$$

$$\mathcal{H} \approx H_0 \sqrt{\Omega_{i0} e^{-\alpha_i x}} = \begin{cases} H_0 \sqrt{\Omega_{\text{rad}0}} e^{-x} & \alpha_{\text{rad}} = 2 \\ H_0 \sqrt{\Omega_{\text{M}0}} e^{-x/2} & \alpha_{\text{M}} = 1 \\ H_0 \sqrt{\Omega_{\Lambda0}} e^x & \alpha_{\Lambda} = -2 \end{cases} \quad (27)$$

These equations will be useful when making sure that the implementations are correct. For a thorough derivation, see below, otherwise skip:



### Derivation of sanity checks

We start with the Hubble equation from Eq. (19) and realize that we may write any derivative of  $U$  as

$$\frac{d^n U}{dx^n} = \sum_i (-\alpha_i)^n \Omega_{i0} e^{-\alpha_i x}.$$

We further have:

$$\frac{d\mathcal{H}}{dx} = \frac{H_0}{2} U^{-\frac{1}{2}} \frac{dU}{dx},$$

and

$$\begin{aligned} \frac{d^2 \mathcal{H}}{dx^2} &= \frac{d}{dx} \frac{d\mathcal{H}}{dx} \\ &= \frac{H_0}{2} \left[ \frac{dU}{dx} \left( \frac{d}{dx} U^{-\frac{1}{2}} \right) + U^{-\frac{1}{2}} \left( \frac{d}{dx} \frac{dU}{dx} \right) \right] \\ &= H_0 \left[ \frac{1}{2U^{\frac{1}{2}}} \frac{d^2 U}{dx^2} - \frac{1}{4U^{\frac{3}{2}}} \left( \frac{dU}{dx} \right)^2 \right] \end{aligned}$$

Multiplying both equations with  $\mathcal{H}^{-1} = 1/(H_0 U^{\frac{1}{2}})$  yield the following:

$$\frac{1}{\mathcal{H}} \frac{d\mathcal{H}}{dx} = \frac{1}{2U} \frac{dU}{dx},$$

and

$$\begin{aligned} \frac{1}{\mathcal{H}} \frac{d^2 \mathcal{H}}{dx^2} &= \frac{1}{2U} \frac{d^2 U}{dx^2} - \frac{1}{4U^2} \left( \frac{dU}{dx} \right)^2 \\ &= \frac{1}{2U} \frac{d^2 U}{dx^2} - \left( \frac{1}{\mathcal{H}} \frac{d\mathcal{H}}{dx} \right)^2 \end{aligned}$$

We now make the assumption that one of the density parameters dominate  $\Omega_i \gg \sum_{j \neq i} \Omega_j$ , enabling the following approximation:

$$U \approx \Omega_{i0} e^{-\alpha_i x}$$

$$\frac{d^n U}{dx^n} \approx (-\alpha_i)^n \Omega_{i0} e^{-\alpha_i x},$$

from which we are able to construct:

$$\frac{1}{\mathcal{H}} \frac{d\mathcal{H}}{dx} \approx \frac{-\alpha_i \Omega_{i0} e^{-\alpha_i x}}{2\Omega_{i0} e^{-\alpha_i x}} = -\frac{\alpha_i}{2},$$

and

$$\begin{aligned} \frac{1}{\mathcal{H}} \frac{d^2 \mathcal{H}}{dx^2} &\approx \frac{\alpha_i^2 \Omega_{i0} e^{-\alpha_i x}}{2\Omega_{i0} e^{-\alpha_i x}} - \left( \frac{\alpha_i}{2} \right)^2 \\ &= \frac{\alpha_i^2}{2} - \frac{\alpha_i^2}{4} = \frac{\alpha_i^2}{4} \end{aligned}$$

which are quantities which should be constant in different regimes and we can easily check if our implementation of  $\mathcal{H}$  is correct, which is exactly what we sought.

parameter, here  $x$ . The density evolution is implemented as:

$$\Omega_n = e^{-\alpha_n x} \Omega_{n0} \mathcal{H}_{\text{rat}}^2 \quad (28)$$

where we have defined the ratio  $\mathcal{H}_{\text{rat}} \equiv H_0/\mathcal{H}$ , and the new index  $n$  are all the densities:  $n \in \{b, c, \gamma, \nu, \Lambda, k\}$ . We also implement functions to solve for the luminosity distance (Eq. (15)), angular distance (Eq. (14)), and the conformal distance (Eq. (12)).

#### 2.2.1. ODEs and Splines

The differential equations for  $\eta$  (Eq. (16)) and  $t$  (Eq. (17)) are solved numerically as ordinary differential equations (ODEs) with the Runge-Kutta 4 as advancement method. The equations are solved for  $x \in [-20, 5)$ . As initial condition we would like  $\eta(-\infty)$  which is obviously not possible to calculate, so we pick some very early time and use the analytical approximation in the radiation dominated era, which yield:

$$\eta(x_0) = \frac{c}{\mathcal{H}(x_0)}. \quad (29)$$

Likewise for  $t$ , the initial condition is:

$$t(x_0) = \frac{1}{2H(x_0)}. \quad (30)$$

We then proceed by making splines of both  $\eta$  and  $t$  in order to evaluate accurately for any  $x \in [-20, 5)$ .

#### 2.2.2. Fit to supernova data

From our implementations we can make predictions of the luminosity distance at different redshifts  $z$ , according to the discussion in Section 2.1.2. These predictions are compared against real supernova observations, acquired by Betoule et al. (2014). In order to constrain the possible values of  $h$ ,  $\Omega_M$  and  $\Omega_\Lambda$  we find the  $\chi^2$ -value between the luminosity distance of the supernovas and our predictions. The  $\Omega$ -s are sampled with Markov-Chain Monte Carlo sampling using the Metropolis-Hastings algorithm.

The parameters in question are  $\Theta = \{h, \Omega_{M0}, \Omega_{k0}\}$ ,<sup>4</sup> and we denote the observed data  $\mathcal{D}_i = d_L^{\text{obs}}(z_i)$ . We assume the likelihood that the observed data is true, follows a normal distribution, with the observed value as mean, and uncertainty as standard deviation. Mathematically:  $P(\mathcal{D}_i|\Theta) \sim \mathcal{N}(\mathcal{D}_i, \sigma_i^2)$ . The total likelihood is thus the product of all  $N$  data points:

$$\mathcal{L}(\Theta|\mathcal{D}) = \prod_{i=1}^N P(\mathcal{D}_i|\Theta) \propto \exp\left\{-\frac{\chi^2}{2}\right\} \quad (31)$$

The last proportionality follows from the fact that  $P$  is normally distributed and that we use:

$$\chi^2(\Theta) = \sum_{i=1}^N \frac{(d_L(z_i, \Theta) - \mathcal{D}_i)^2}{\sigma_i^2}. \quad (32)$$

We use as prior (the probability that the observed data is true without any further information), a uniform distribution that is 1 if the parameters are within the following ranges (0 otherwise):  $0.5 < h < 1.5$ ,  $0.0 < \Omega_{M0} < 1.0$ ,  $-1.0 < \Omega_{k0} < 1.0$ . These are the absolute ranges of the parameters. According to Bayes' theorem, within these ranges we have that the posterior probability

$$P(\Theta|\mathcal{D}) \propto \mathcal{L}(\Theta|\mathcal{D}) \cdot \text{Prior} = \mathcal{L}(\Theta|\mathcal{D}). \quad (33)$$

<sup>4</sup> Not to be confused with the temperature fluctuations introduced later.

## 2.2. Methods

We have to consider the time evolution of the density parameters, given some present value, as function of our chosen time

Finding the most probable set of parameters  $\Theta$  is equivalent to finding the set with the largest likelihood, which again is similar to finding the set which minimises  $\chi^2$ .

When performing MCMC sampling (with MH-algorithm), we use Eq. (31) as the likelihood function. That means that we would expect normally distributed values of the different parameters,  $\Theta$ . We may from the distributions of each parameter estimate the mean (true value) and a confidence interval from its standard deviation. We may also find the  $1\sigma$  confidence space for the collection of parameters in  $\Theta$ , by considering the distribution of  $\chi^2$ . This is a famous distribution whose  $1\sigma$  interval (for  $k = 3$  degrees of freedom in this case) is given by  $|\chi^2 - \chi^2_{\min}| < 3.53$ .

It is also of interest to say something about whether it is a good fit. It is easy to see from Eq. (32) that if the difference between prediction and observation matches the uncertainties in the observed data, then we have  $\chi^2 \simeq N$ , which is the best fit we can hope for (since we fit to data which has an intrinsic uncertainty already). If  $\chi^2 \ll N$ , then we *over-fit* the model, while if  $\chi^2 \gg N$  then we have an increasingly bad fit. In summary, we may analyse the following quantity

$$\frac{\chi^2}{N} \begin{cases} \ll 1 & \text{over-fitting,} \\ \simeq 1 & \text{good fit,} \\ \gg 1 & \text{bad fit,} \end{cases} \quad (34)$$

in order to determine the goodness of fit.

## 2.3. Results and discussion

### 2.3.1. Tests

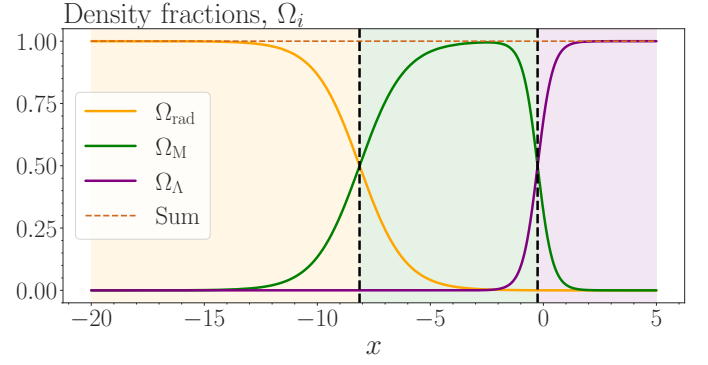
Fig. 1 show the evolution of the density fractions with time. They sum to one across all times which was required. At early times the radiation density dominates (orange line). The intersection between the orange and green lines mark the radiation-matter equality, after which matter is the dominating density. Likewise, the intersection between the green and purple lines mark the matter-dark energy equality, where dark energy (manifested in the cosmological constant) become the dominating density. Time can thus be divided into three regimes; radiation dominated, matter dominated, and dark energy dominated eras, separated by black dotted lines in the plot. Fig. 2 is the sanity check for  $\eta$  showing that its derivative take the desired value of  $c/\mathcal{H}$ .

Fig. 3 is the sanity check confirming that our constructions of  $\mathcal{H}$  and its derivatives converge to the analytical approximation in the different regimes. The second derivative, as shown in blue, takes the value of 1 in the radiation regime, 1/4 in the matter regime and 1 in the dark energy regime. Similarly, the first derivative, as shown in red, take the value -1 in the radiation regime, -1/2 in the matter regime and 1 in the dark energy regime. This is well in accordance with the analytical approximations put forth in section Section 2.1.4.

These sanity checks are confirmations that the implementations yield the same result as the analytical approximation in the different regimes for various constructions of  $\eta$  and  $\mathcal{H}$  and their derivatives.

### 2.3.2. Analysis

In Section 2.1.3 we indicate how we can calculate the radiation-matter equality (RM-equality), matter-dark energy equality (ML-equality), when the acceleration of the universe started, the age of the universe and the conformal time today. The result is shown in Table 1. We note that the equalities is in accordance



**Fig. 1.** Density fractions  $\Omega_i$  as function of  $x$ . For low  $x$ , radiation dominates, before matter dominates and dark energy has just become the dominant energy density today  $x = 0$ , and will continue to dominate into the future. The sum of densities sums to one across all times, as required (brown dotted line). The black dotted lines are the radiation-matter equality at  $x = -8.13$  and the matter-dark energy equality at  $x = -0.26$ , both stated in Table 1. The domination of each regime is shown as a shaded background with similar colour as its respective graph.

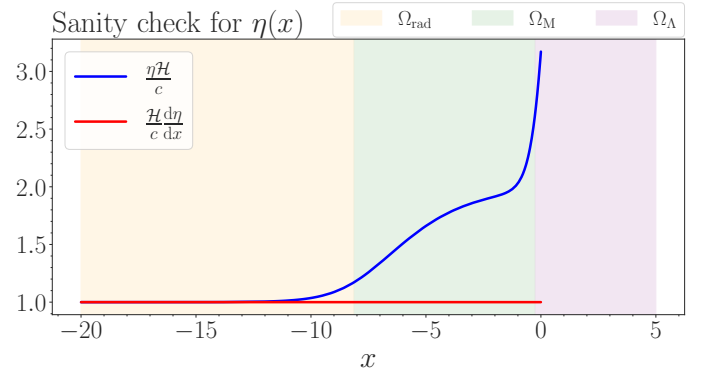


**Fig. 2.** Sanity check for  $\eta$ .

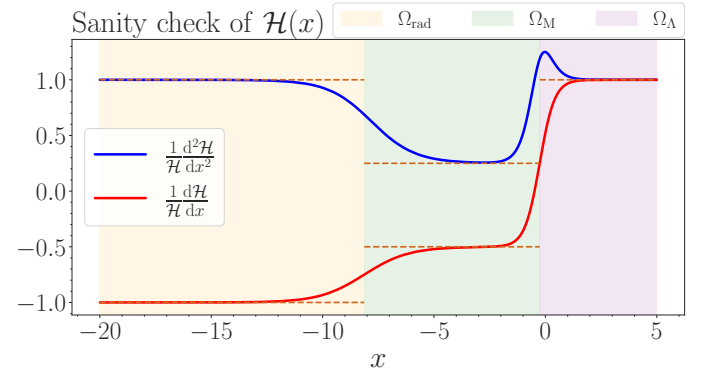


**Fig. 3.** Sanity check for  $\mathcal{H}$ , showing that the second derivative (blue) converge to the analytical expressions shown as brown dotted lines in the different regimes. The first derivative (red) converge to its analytical values in the same regimes, which again are shown with a shaded colour.

with the sanity checks, and the age of the universe today (in cosmic time) is about 13.9 Gyr. We also note that the acceleration onset is slightly before the matter-dark energy equality at  $x = -0.49$  and  $x = -0.26$  respectively.

The conformal Hubble factor,  $\mathcal{H}$ , is plotted against time,  $x$ , in Fig. 4. It is decreasing in the radiation and matter regimes

Quantity	$x$	$z$	$t$
RM-equality	-8.13	3400	$51 \cdot 10^3$ yr
ML-equality	-0.26	0.29	10.378 Gyr
Accel. start	-0.49	0.63	7.752 Gyr
Age of universe	0.00	0.00	13.858 Gyr
Conformal time	0.00	0.00	46.319 Gyr

**Table 1.** Important quantities in the evolution of the universe. RM stands for radiation-matter and ML for matter-dark energy.

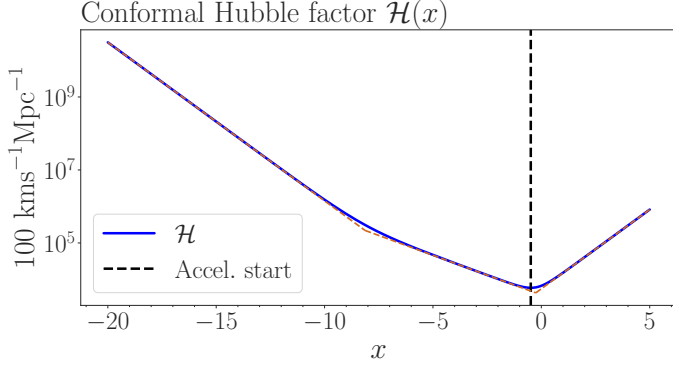


**Fig. 4.**  $\mathcal{H}$  as function of  $x$ . It is decreasing in the radiation and matter regimes, and increasing in the dark energy regime, tightly following its analytical approximation in each regime.

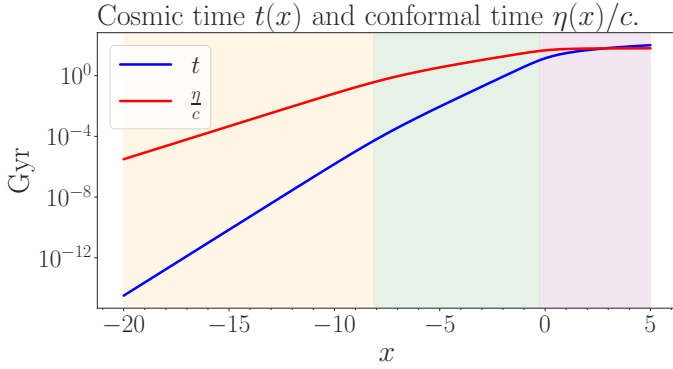


**Fig. 5.** Cosmic time (in blue) and conformal time (red).

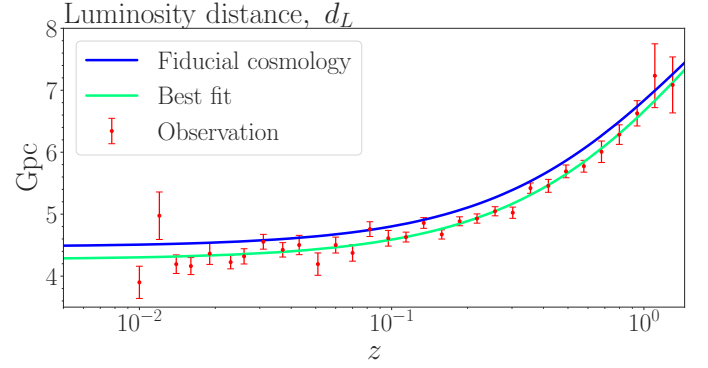
and increasing in the dark energy regime, with a turnover at the acceleration onset, which is marked with a black dotted line in the figure.

Fig. 5 show the cosmic time  $t$  and the conformal time  $\eta/c$ . The cosmic time is the age of the universe at any given time/size  $x$ . The low values for the cosmic time at early times suggest a rapid increase of the size of the Universe in a short cosmic time. This is supported by the conformal Hubble factor in Fig. 4 which is large for low  $x$ . The expansion rate of the universe decelerates until the acceleration onset, from which it accelerates. This acceleration means that the rate of expansion of the Universe will at some point surpass the conformal horizon, effectively decreasing the observable Universe.

The results of the supernova fitting, outlined in Section 2.2.2, is summarised in Table 2. The parameter values that maximises the likelihood (minimising)  $\chi^2$  are:  $h = 0.702$ ,  $\Omega_{M0} = 0.259$  and  $\Omega_{k0} = 0.274$ . We also compute the posterior probability distribution function obtained from Eq. (33) which we have assumed to be normally distributed. From this we obtain a mean value, but also a  $1\sigma$  confidence interval, which are:

	$h$	$\Omega_{M0}$	$\Omega_{k0}$
Best: $\min \chi^2$	0.702	0.259	0.067
Posterior	0.701	0.247	0.107
$1\sigma$ confidence	0.006	0.110	0.274

**Table 2.** Best and fitted values. The best fit values are those that actually minimise the  $\chi^2$ -value, which consequently are the most probable values. The fitted values are obtained as the mean and standard deviations of the posterior pdfs of the parameters respectively.



**Fig. 6.** The luminosity distance predicted using the fiducial cosmology in blue, against observations of actual supernovas in red (or rather the confidence interval of the observations). The green line is found from computing the luminosity distance using a cosmology of the best fit parameters from the supernova fitting;  $h = 0.702$ ,  $\Omega_{b0} = 0.05$ ,  $\Omega_{c0} = 0.209$ ,  $\Omega_k = 0.067$ ,  $N_{\text{eff}} = 3.046$ ,  $T_{\text{CMB}} = 2.7255\text{K}$ . Notice the  $x$ -axis is now the redshift  $z = e^x - 1$ .

$$\begin{aligned}
 h &= 0.701 \pm 0.006 \\
 \Omega_{M0} &= 0.247 \pm 0.110 \\
 \Omega_{k0} &= 0.107 \pm 0.274
 \end{aligned} \tag{35}$$

Let's first see for ourselves if these values make sense or not, just with by-eye comparison. Fig. 6 shows the supernova data as red error bars, with the predictions from the fiducial cosmology plotted above it, alongside the best fit parameter values. The quantity plotted is the luminosity distance divided by redshift,  $d_L/z$  for better comparison. We notice the accordance between the two, and also note that the  $x$ -axis in this plot is the redshift  $z$  instead of the logarithm of the scale factor. This means that earlier times are to the right in the plot (high redshift), as opposed to the other plots. Immediately we see that the best fit parameters seems to do a better job at staying within the red error bars. However, the fiducial cosmology is also good. Furthermore, the fiducial cosmology stays well within the  $1\sigma$  confidence interval found from the posterior pdfs. It is also worth noting that the uncertainties on some observed values are large.

Now let's turn to how we have constrained the parameters. Fig. 7 shows the  $\chi^2$ -values found from Eq. (32), constrained to  $1\sigma$  interval. The black dotted line represent a flat universe, where the matter and dark energy are the main constituents of the universe. The supernova data originate in close temporal proximity to us, we thus assume that the contribution from the radiation density is negligible for making constraints on  $\Omega_{M0}$  and  $\Omega_{k0}$  today. Having only  $\Omega_{M0}$ ,  $\Omega_{k0}$  and  $\Omega_{\Lambda0}$ , where only two of them are free yield:  $\Omega_{k0} = 1 - (\Omega_{M0} + \Omega_{\Lambda0})$ , which fixes the relationship,



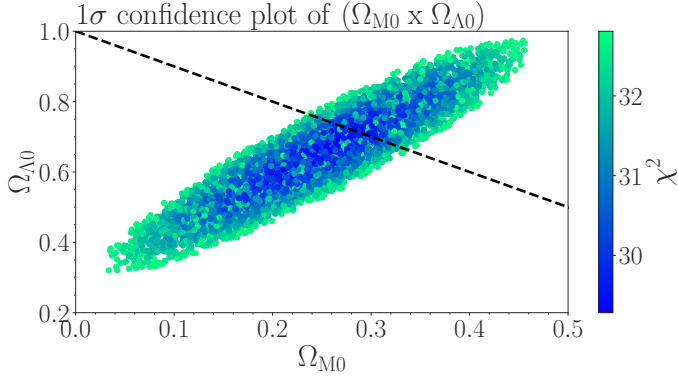


**Fig. 7.** Scatter plot showing the  $\chi^2$ -values of the luminosity distance  $d_L$  between the observed values  $\mathcal{D}$  and the sampled values, as function of  $\Omega_{M0}$  and  $\Omega_{A0}$ . The data shown is the  $1\sigma$  confidence region. The black dotted line signifies a flat universe.

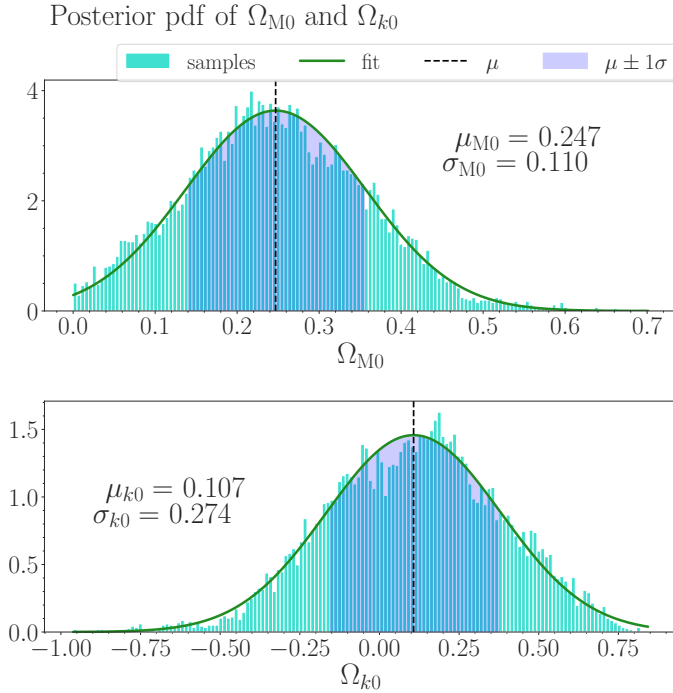


**Fig. 8.** Posterior probability distributions (pdfs) of  $\Omega_{M0}$  and  $\Omega_{k0}$  as result of the MCMC sampling. The samples are shown in turquoise and the constructed pdfs in green. The mean  $\mu$  is shown as a black dotted line, with the  $1\sigma$  confidence interval in shaded blue ( $\mu \pm 1\sigma$ )

so that it does not matter which two of them we constrain, as the constraint on the third automatically follows.<sup>5</sup>

From the sampled values we then generate the posterior pdf by making a histogram of all the samples. This is seen for  $\Omega_{M0}$  and  $\Omega_{k0}$  in Fig. 8 and for  $H_0$  in Fig. 9, all histograms are in turquoise. From the samples we also find their respective mean and standard deviation, from which we plot a green Gaussian curve on top of the histogram. The means are indicated with black dotted lines, and the  $1\sigma$  confidence regions are shaded in blue. Both quantities are also stated in text in each plot, in accordance with those presented in Table 2. From inspection, we see that the histograms are quite close to being normally distributed, so the fitted Gaussian is a good fit.

<sup>5</sup> This is why we are able to put constraints on  $\Omega_{A0}$  even though this parameter is not (directly) sampled in the MCMC sampling.

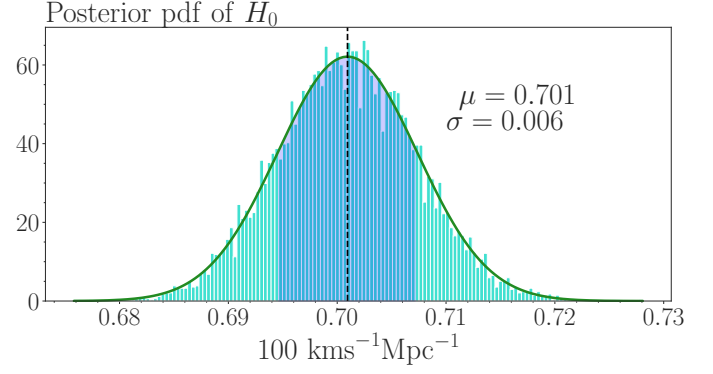


**Fig. 9.** Posterior probability distribution (pdf) of  $H_0$  as result of the MCMC sampling.

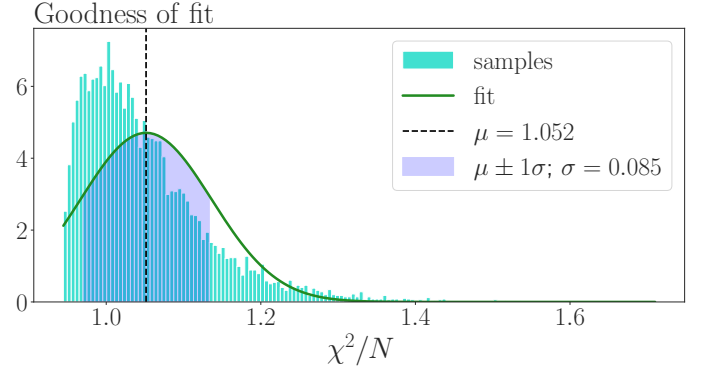


**Fig. 10.** Goodness of fit, showing the mean value of  $\chi^2/N$  is close to 1, which is a good fit. The Gaussian function does not seem to encapsulate behaviour of the samples.

Discussing the goodness of the fit further, we may turn to the criterion from Eq. (34). Fig. 10 show a histogram of the sampled  $\chi^2$  values, divided by  $N$ . In sight of prior discussion, the mean value of  $\chi^2/N$  is 1.052, which is not that much larger than 1. Thus, we deduce that the fit is good. Although we also see from the figure that  $\chi^2/N$  deviates significantly from the Gaussian curve in green.

Nevertheless, we shall continue to use the fiducial cosmology from Betoule et al. (2014), but now we have some viable constraints on them.

### 3. Recombination History

The main goal of this section is to investigate the recombination history of the universe. This can be explained as the point in time when photons decouple from the equilibrium of the opaque early universe. This is known as the *time of last scattering*,<sup>6</sup> and these photons are what we today observe as the CMB. This period of the history of the universe is thus crucial for understanding the CMB.

We will start by calculating the free *electron fraction*  $X_e$ , from which we may find the *optical depth*  $\tau$ . This again enables us to compute the *visibility function*,  $g$ , and the *sound horizon*,  $s$ . The latter will be of great importance later.

Recombination happens because the expansion of the Universe cools it down, making the photons less energetic, which in turn make each interaction in the primordial plasma less energetic. At some point, hydrogen atoms are able to form, reduc-

<sup>6</sup> Which is exactly what the name suggests.

ing the number of free electron, hence reducing photon interactions, until they scatter for the last time. We will determine the time of recombination from the free electron fraction, which indirectly tell us how large portion of the free electrons have (re)-combined.<sup>7</sup> Due to the decrease of free electrons, photons interact less with them. At some point, photons scatter for the last time, and this information is encapsulated in the visibility function.

### 3.1. Theory

In order to explain the inventory of the Universe, we need to understand how the distribution of different species change over time. This is governed by the *Boltzmann equation*,

$$\frac{df}{dt} = C[f], \quad (36)$$

where  $f(\mathbf{x}, \mathbf{p}, t)$ <sup>8</sup> is the distribution function of a given species.  $C[f]$  are the collision terms, which depends on the species through the same distribution function  $f$ . Due to the function dependencies of  $f$  we are able to generally expand it into (Dodelson & Schmidt 2020, Eq. 3.33):

$$\frac{df}{dt} = \frac{\partial f}{\partial t} + \frac{\partial f}{\partial x^i} \frac{dx^i}{dt} + \frac{\partial f}{\partial p} \frac{dp}{dt} + \frac{\partial f}{\partial \hat{p}^i} \frac{d\hat{p}^i}{dt} = C[f], \quad (37)$$

where  $p = |\mathbf{p}|$  and  $\hat{p} = \mathbf{p}/p$ .

Before recombination, the equilibrium between protons, electrons and photons is governed by the following interaction, from Weinberg (2008)<sup>9</sup>:

$$e^- + p^+ \rightleftharpoons H^* + \gamma. \quad (38)$$

Here, a proton and an electron interact to (i): Form an excited hydrogen atom, which then decays and emits a photon, or (ii): A photon excites and split a hydrogen atom into a free electron and a proton through *Compton scattering*.<sup>10</sup> Eq. (38) is a reaction of the form  $1 + 2 \rightleftharpoons 3 + 4$ , and we have from Winther et al. (2023) that the Boltzmann equation for such a reaction is:

$$\frac{1}{n_1 e^{3x}} \frac{d(n_1 e^{3x})}{dx} = -\frac{\Gamma}{H} \left( 1 - \frac{n_3 n_4}{n_1 n_2} \left( \frac{n_1 n_2}{n_3 n_4} \right)_{\text{eq}} \right), \quad (39)$$

where  $n_i$  are the number densities of the reactants,  $\Gamma$  is the reaction rate and  $H$  the Hubble parameter (expansion rate of the universe). If the reaction rate is much larger than the expansion rate of the universe,  $\Gamma \gg H$ , then Eq. (38) ensures equilibrium between protons, electron and photons. When  $\Gamma$  drops below  $H$ , then the expansion rate becomes dominant and the reaction rate

<sup>7</sup> As with any (hopefully good) article on the subject, we ought to say that recombination is a funny wording, as this is the first time in the history of the Universe that protons and electrons combine to form hydrogen.

<sup>8</sup> Given in *phase-space coordinates*:  $(x^\mu, P^\mu)$ , where an index to  $x$  indicates spatial coordinate, not time.

<sup>9</sup> Where  $H^*$  denotes excited states of hydrogen which will decay into neutral hydrogen.

<sup>10</sup> Elastic scattering of photons is technically Thomson scattering, but Compton scattering is a more general term and will be used (Dodelson & Schmidt (2020)). This is also why we later use the Thomson cross section  $\sigma_T$ . The reaction is when a photon scatters of an electron, and possibly energises it enough to break out of the hydrogen atom, if already bound:

$$\gamma + e^- \rightleftharpoons \gamma + e^-.$$

is unable to sustain equilibrium. This happens when the temperature of the Universe becomes lower than the binding energy of hydrogen, hence stable neutral hydrogen is able to form.<sup>11</sup> As a consequence, the photons *decouple* from the protons and electrons. When  $\Gamma \ll H$ , there are practically no interactions and the number density becomes constant for a comoving volume. Massive particles *freeze out* and their abundance become constant.

#### 3.1.1. Hydrogen recombination

We express the electron density through the free electron fraction  $X_e \equiv n_e/n_H = n_e/n_b$  where we have assumed that hydrogen make up all the baryons ( $n_b = n_H$ ). We also ignore the difference between free protons and neutral hydrogen. From Callin (2006) we obtain:

$$n_b = \frac{\rho_b}{m_H} = \frac{\Omega_b \rho_c}{m_H} e^{-3x}, \quad (40)$$

where  $m_H$  is the mass of the hydrogen atom, and  $\rho_{\text{crit}}$  the critical density today as defined earlier. Before recombination, no stable neutral hydrogen is formed, thus the electron and baryon density is the same, i.e. there are only free electrons so  $X_e \simeq 1$ . When in equilibrium, the r.h.s. of Eq. (39) reduces to 0, which is called the *Saha approximation*:

$$\frac{n_3 n_4}{n_1 n_2} \left( \frac{n_1 n_2}{n_3 n_4} \right)_{\text{eq}} = 1 \quad (41)$$

The solution is in this regime described by the *Saha equation*, which from Dodelson & Schmidt (2020) in physical units is:

$$\frac{X_e^2}{1 - X_e} = \frac{1}{n_b} \left( \frac{k_B m_e T_b}{2\pi \hbar^2} \right)^{3/2} e^{-\epsilon_0/k_B T_b}, \quad (42)$$

where  $\epsilon_0 = 13.6$  eV is the ionisation energy of hydrogen. The Saha equation is only a good approximation when  $X_e \simeq 1$ . Thus for  $X_e < (1 - \xi)$ ,<sup>12</sup> which corresponds to the period during and after recombination, we have to make use of the more accurate *Peebles equation*. From Callin (2006):

$$\frac{dX_e}{dx} = \frac{C_r(T_b)}{H} \left[ \beta(T_b)(1 - X_e) - n_H \alpha^{(2)}(T_b) X_e^2 \right], \quad (43)$$

<sup>11</sup> Well, it is really not as simple, as neutral hydrogen is obtained from excited hydrogen and how this process go about is non-trivial. As we ignore re-ionisation, I will not delve into this. However, both (Weinberg 2008, p. 113-129), (Dodelson & Schmidt 2020, p. 95-99) and Winther et al. (2023) elaborate further on this.

<sup>12</sup> Where  $\xi$  is some small tolerance, which have to be defined in some numerical model for when to abandon the Saha equation and use the more accurate, but computationally more expensive Peebles equation. This is typically  $\xi = 0.001$

where

$$C_r(T_b) = \frac{\Lambda_{2s-1s} + \Lambda_\alpha}{\Lambda_{2s-1s} + \Lambda_\alpha + \beta^{(2)}(T_b)}, \quad (43a)$$

$$\Lambda_{2s-1s} = 8.227 \text{ s}^{-1}, \quad (43b)$$

$$\Lambda_\alpha = \frac{1}{(\hbar c)^3} H \frac{(3\epsilon_0)^3}{(8\pi)^2 n_{1s}}, \quad (43c)$$

$$n_{1s} = (1 - X_e) n_H, \quad (43d)$$

$$n_H = (1 - Y_p) \frac{3H_0^2 \Omega_{b0}}{8\pi G m_H} e^{-3x}, \quad (43e)$$

$$\beta^{(2)}(T_b) = \beta(T_b) e^{3\epsilon_0/4k_B T_b}, \quad (43f)$$

$$\beta(T_b) = \alpha^{(2)}(T_b) \left( \frac{k_B m_e T_b}{2\pi \hbar^2} \right)^{3/2} e^{-\epsilon_0/k_B T_b}, \quad (43g)$$

$$\alpha^{(2)}(T_b) = \frac{\hbar^2}{c} \frac{64\pi}{\sqrt{27}\pi} \frac{\alpha^2}{m_e^2} \sqrt{\frac{\epsilon_0}{k_B T_b}} \phi_2(T_b), \quad (43h)$$

$$\phi_2(T_b) = 0.448 \ln \left( \frac{\epsilon_0}{k_B T_b} \right). \quad (43i)$$

The Peebles equation takes into account that the energy (excitation) of hydrogen formed through Eq. (38) vary, and that decays take place until we reach the  $n = 2$  level (first excited state), denoted by  $^{(2)}$  in Eq. (43a)- Eq. (43i). Recombination to the ground state is not relevant, as this leads to an ionised photon which immediately ionises a neutral hydrogen atom (Dodelson & Schmidt 2020, p. 97). The  $C_r$  is the probability that singly ionised hydrogen is reionised further, where  $\beta^{(2)}$  and  $\beta$  are the collisional ionisations from the first ionised state and ground state respectively.  $\alpha^{(2)}$  is the recombination rate to excited states. For more detailed description of these terms, see Ma & Bertschinger (1995). Because of this non-trivial path into the ground state, and the large photon to baryon number ratio, recombination happens later than when the temperature of the universe correspond to exactly the binding energy of neutral hydrogen (Callin (2006)), which was our initial expectation.

We find  $X_e$  by solving Eq. (42) for  $X_e > (1 - \xi)$  and Eq. (43) for  $X_e < (1 - \xi)$ . In theory, it is possible to solve the Peebles equation at very early times. However, this is challenging since Eq. (39) is a strong attractor for large temperatures, making it very stiff. This results in unstable numerical solutions at early times (high temperatures), hence the Saha approximation.

### 3.1.2. Visibility

Visibility is a concept tied to the optical depth and mean free path of a medium. The two latter are inversely proportional to each other. The mean free path is the average distance a photon travels before its direction is changed (often by scattering). Thus, a small mean free path results in a lot of collision across short distances, which occurs in optically thick media. The optical depth as a function of conformal time is defined as Winther et al. (2023):

$$\tau = \int_\eta^{\eta_0} n_e \sigma_T e^{-x} d\eta', \quad (44)$$

where  $n_e$  is the electron density and  $\sigma_T$  is the Thompson cross-section. Optical depth can in a classical sense be thought of as how far we can see into a substance or medium. The medium in question here is actually spacetime itself, since we integrate across the conformal time from some time  $\eta$  up until today:  $\eta_0$ . Therefore, the optical depth today is zero, since photons have

had no time to actually travel through any medium. The medium we consider is the spacetime of our past light-cone when we “look back in time”. In differential form, restoring original units, this is:

$$\frac{d\tau}{dx} = -\frac{cn_e \sigma_T e^x}{\mathcal{H}}. \quad (45)$$

From this we define the visibility function,  $g$ :

$$g = -\frac{d\tau}{d\eta} e^{-\tau} = -\mathcal{H} \frac{d\tau}{dx} e^{-\tau} \\ \tilde{g} \equiv -\frac{d\tau}{dx} e^{-\tau} = \frac{g}{\mathcal{H}}, \quad (46)$$

where  $\tilde{g}$  is in terms of the preferred time variable,  $x$ . Notable thing about the visibility function  $\tilde{g}$  is that it is a true probability distribution, describing the probability density of some photon to last have scattered at time  $x$ . Because of this, we have that  $\int_{-\infty}^0 \tilde{g}(x) dx = 1$ . We also take note of the derivative of the visibility function:

$$\frac{d\tilde{g}}{dx} = e^{-\tau} \left[ \left( \frac{d\tau}{dx} \right)^2 - \frac{d^2\tau}{dx^2} \right] \quad (47)$$

### 3.1.3. Sound horizon

Let's take a small step back and consider the situation of the early Universe. Before any decoupling, the photons and electrons are coupled through Thompson scattering, and protons and electrons are coupled through coulomb interactions. Because of this, photons interact with baryons and move alongside with them as one fluid, in which wave propagates with a speed  $c_s$ , from Dodelson & Schmidt (2020):

$$c_s \equiv c [3(1 + R)]^{-\frac{1}{2}} \quad ; \quad R \equiv \frac{3\Omega_b}{4\Omega_\gamma}, \quad (48)$$

where  $R$  is the *baryon-to-photon energy ratio*. By the definition of  $R$ , if the baryon density is negligible compared to the radiation density,  $R \sim 0$ , and we recover the wave propagation speed in a relativistic fluid:  $c_s = 3^{-1/2}$  (Dodelson & Schmidt (2020)). The total distance such a wave would have travelled in a time  $t$  (since the beginning of the Universe) is called the *sound horizon*, found by simply integrating  $c_s$  through time, accounting for the expansion of space itself by including a factor  $e^{-x}$ :

$$s = \int_0^t c_s e^{-x} dt = \int_{-\infty}^x \frac{c_s}{\mathcal{H}} dx, \quad (49)$$

where the variables are changed to  $x$ . On differential form:

$$\frac{ds}{dx} = \frac{c_s}{\mathcal{H}}, \quad (50)$$

which is a straightforward differential equation to solve given some initial conditions.

## 3.2. Methods

### 3.2.1. Computing $X_e$

First things first, we need to compute the free electron fraction  $X_e$ . We are for the most part not interested in things happening in the future here, so the temporal range of choice will be  $x \in [-20, 0)$  where  $x = 0$  is today, and  $x = -20$  is sufficiently

long ago, so that the range encapsulates the effects studied here. In the early Universe, the energies are so high that all baryonic matter is in the form of free electron,  $X_e \simeq 1$ , so we will start by solving the Saha equation, Eq. (42). We continue to solve equation Eq. (42) as long as  $X_e > 1 - \xi$  where we use  $\xi = 0.001$ .

If we define:

$$K \equiv \frac{1}{n_b} \left( \frac{k_B m_e T_b}{2\pi\hbar^2} \right)^{3/2} e^{-\epsilon_0/k_B T_b}, \quad (51)$$

then equation Eq. (42) takes the form  $X_e^2 + KX_e - K = 0$ , which is solved as a normal quadratic equation, where  $a = 1$ ,  $b = K$  and  $c = -K$ . Since  $0 \leq X_e \leq 1$  we choose the positive solution, given by:

$$X_e = \frac{-K + \sqrt{K^2 + 4K}}{2} = \frac{K}{2} \left( -1 + \sqrt{1 + 4K^{-1}} \right) \quad (52)$$

This solution has the potential to become numerically unstable if the parenthesis is close to zero, i.e. for  $K \gg 1$ . We then make use of the approximation  $\sqrt{1 + 4K^{-1}} \approx 1 + (2K^{-1})$  for  $|4K^{-1}| \ll 1$ , which ensures  $X_e \simeq 1$  for very high temperatures (large  $K$ ).

We continue to solve the Peebles equation as stated in Eq. (43), where the r.h.s. is implemented sequentially as Eq. (43a)- Eq. (43i) in reverse order. The initial condition is the last computed electron fraction above the cut-off:  $X_{e0} = \min(X_e > 1 - \xi)$  as found from the Saha equation. It is solved for the x-range not solved by the Saha equation. One thing to notice is that for late time,  $T_b$  becomes small, meaning that  $e^{\epsilon_0/k_B T_b}$  becomes enormous. This term is found in Eq. (43f), and we solve it by setting  $\beta^{(2)}(T_b) = 0$  if  $\epsilon/k_B T_b > 200$ , in order to avoid overflow.

Having found  $X_e$  for the entire x-range, we compute  $n_e$  and spline both results.

### 3.2.2. Computing $\tau$ and $\tilde{g}$

With  $n_e$  we are able to solve the optical depth as defined in Eq. (45). The initial condition for this equation is that the optical depth today is zero:  $\tau(x = 0) = 0$ , meaning we have to solve this backwards in time. This is done by using the negative differential:

$$\frac{d\tau_{\text{rev}}}{dx_{\text{rev}}} = -\frac{d\tau}{dx} = \frac{cn_e\sigma_T e^x}{\mathcal{H}}, \quad (53)$$

and solving for positive  $x_{\text{rev}}$ :  $x_{\text{rev}} \in [0, 20]$ . In order to undo this reversal, we map  $\tau = -\tau_{\text{rev}}$  to its corresponding  $x = -x_{\text{rev}}$ . Having found  $\tau$ , we find its derivative by solving equation Eq. (45), and further find the visibility function from Eq. (46) and its derivative from Eq. (47). We ensure that  $\int_{-\infty}^0 \tilde{g} dx = 1$  as a sanity check. All of these four quantities are splined, and their derivatives are obtained numerically.

In order to solve Eq. (49) for the sound horizon, we choose initial conditions  $s_i = c_{s,i}/\mathcal{H}_i$  where the subscript  $i$  denote a very early time (in our case when  $x = -20$ ). We are then able to solve the differential equation for the sound horizon, Eq. (50), numerically and then spline the result.

### 3.2.3. Analysis

Having splines for the relevant quantities enables us to compute some important times in the early universe. Firstly, the *last scattering surface* is the time when most photons scattered for the

Phenomenon	$x$	$z$	$t$ [Myr]	$r_s$ [Mpc]
Last scattering	-6.9853	1079.67	0.3780	145.31
Recombination	-6.9855	1079.83	0.3779	145.29
Saha	-7.1404	1260.89	0.2909	131.03

**Table 3.** The times of last scattering and recombination given in terms of  $x$ , the redshift  $z$ , the cosmic time  $t$  and the sound horizon  $r_s$ . Also included is the time of recombination found using the Saha approximation only.

last time, and decoupled from the plasma. This is not expected to have happened instantly, but recalling that the visibility function  $\tilde{g}$  is a probability distribution function for when photons last scattered, we simply use the peak of this function as the definition of the last scattering surface.

Further, we want to find a time for when recombination happened, i.e. when free electron was captured by protons to form hydrogen atoms. This coincides with the reduction of the free electron fraction, and we will use  $X_e = 0.1$  as the definition for when recombination happened. These numbers can also be computed using only the Saha approximation, for comparison. We also compute the sound horizon at these decouplings:  $r_s = s(x_{\text{dec}})$ .

The last thing we want to compute is the freeze out abundance of free electrons, i.e. the free electron abundance today, which is found by evaluating the spline for  $X_e$  at  $x = 0$ .

## 3.3. Results and discussion

### 3.3.1. Times and sound horizon

The relevant times for last scattering, recombination and Saha recombination are obtained as explained in Section 3.2.3, and presented in Table 3. These times are given in terms of  $x$ , the redshift  $z$  and the cosmic time  $t$  (in Myr). The sound horizon is given in units of megaparsecs (Mpc). Last scattering occurred when  $x = -6.9853$ , at redshift  $z = 1079.67$ , which is slightly after recombination when  $x = -6.9855$  at redshift  $z = 1079.83$ . If the Saha approximation was valid when the electron fraction dropped, recombination would have happened when  $x = -7.1404$  at redshift 1260.89 which is significantly earlier. However, this is not the case since photons drop out of equilibrium with the primordial plasma as soon as hydrogen begins to form, and the free electron fraction is reduced. Thus, this number may only be used for comparison.

### 3.3.2. Free electron fraction

Fig. 11 shows the free electron fraction  $X_e$  as a function of  $x$  found using both the Saha and Peebles equation, as explained in Section 3.2.1, in blue. Also shown is the results found from the Saha equation only, which tends to zero a lot faster. This is used for comparison only, as we have already stated that the Saha approximation is only valid for  $X_e \simeq 1$ . The time of recombination is shown for both cases, which for the Saha approximation happens significantly earlier than what is the actual case. The Peebles solution falls off gradually, and converges towards a constant value, which is the present day abundance of free electrons (freeze out abundance). This is found to be  $X_e(x = 0) = 0.0002$ , shown as a brown dashed line in Fig. 11.

Since the Peebles equation is a solution of the Boltzmann equation, it takes into account the particle interaction with



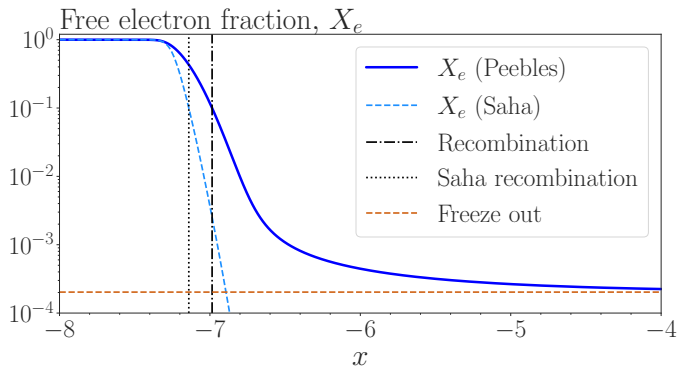


**Fig. 11.** The free electron fraction  $X_e$  as function of  $x$ , found from the Saha and Peebles equation (blue). The result using only the Saha equation is shown in dashed light blue. The time of recombination is shown as a dashed black line. Likewise, recombination in the Saha approximation is shown as a dotted black line, appearing earlier. The freeze out abundance of hydrogen (the present value) is shown as a brown dashed line.

changing abundance, after the photons decouple from the primordial plasma. It is thus expected that this will result in a much more gradual fall off of the free electron fraction, just as we observe in Fig. 11.

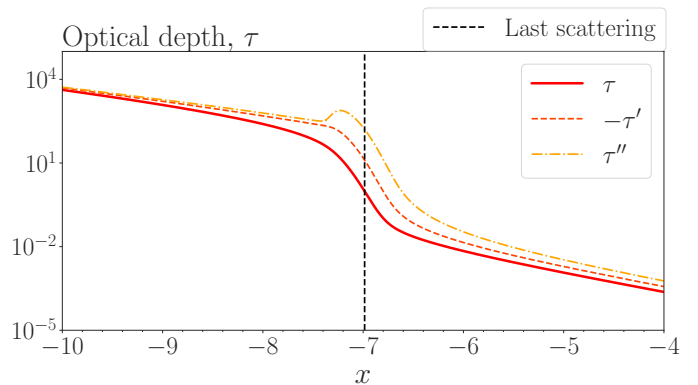
### 3.3.3. Visibility

Fig. 12 shows the optical depth and its first two derivatives. This is a function of the time  $x$ , and the optical depth at some value is the integral of Eq. (44) from that time until today; it is cumulative. The surface of last scattering is shown with a black dashed line, before which the primordial plasma is optically thick, meaning the photons have a short mean free path. The decrease of the optical depth means that the photons gradually travel longer distances before interacting with free electrons. There are two processes going on here; the expansion of space itself, and the formation of neutral hydrogen. Both of which contribute to the increased mean free path of the photons. The contribution from the expansion of space is slow compared to the seemingly rapid change in the free electron fraction once neutral hydrogen is able to form. Thus, the rapid decrease of free electrons, as seen in Fig. 11 makes the mean free paths of photon to increase beyond the horizon. This effectively enable them to travel through space without interacting with matter, and this is what we observe as the CMB today - the Universe becomes transparent. This sudden decrease of optical depth is clearly seen in Fig. 12, both in  $\tau$  itself, but also in its derivatives.

Another way of arriving at similar conclusions is by considering the visibility function in Fig. 13. Here,  $\tilde{g}$  is shown in green along with its derivatives. The scaling follow that of Callin (2006), in order to fit the graphs into the same figure.  $\tilde{g}$  describes the probability that a photon reaching us today scattered at time  $x$ . The peak of this function indicates the time were the *most* photons scattered for the last time, and is thus used as a definition of the last scattering surface. The visibility function is skewed forward in time.

### 3.3.4. General discussion

One key thing to keep in mind is that recombination did not happen instantaneously, but rather over a relatively short period in which neutral hydrogen formed rapidly. This caused a rapid de-



**Fig. 12.** The optical depth  $\tau$  and its first and second derivatives as functions of  $x$ . The time of last scattering is shown as a dashed black line, before which the Universe was optically thick.

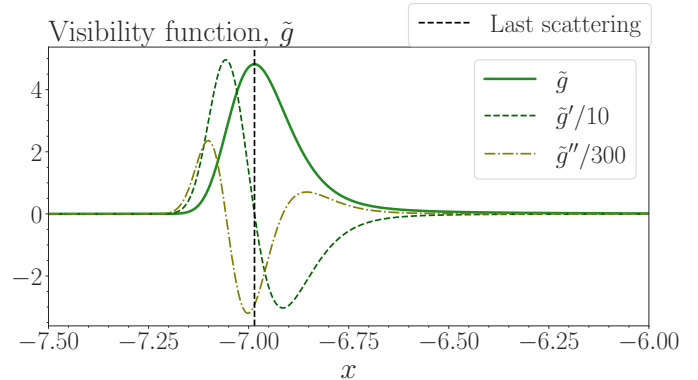


**Fig. 13.** The visibility function  $\tilde{g}$  and its first and second derivatives as functions of  $x$ . The time of last scattering is shown as a dashed black line, which by definition coincides with the peak of the visibility function.

crease of the free electron fraction, which again caused the optical depth to decrease by several magnitudes. In the same period, we see a that the visibility function is non-zero, meaning the probability of last scattering is (relatively) high in this period. The times quoted in Table 3 are times that arise from our quite rigid, but fair definition of last scattering and recombination. However, these times do not encapsulate the duration of the abovementioned period. One could also define the last scattering surface as the time when  $\tau = 1$  which is the transition between optically thick and optically thin media (when the photon travels exactly one mean free path before scattering). However, the visibility function is arguably a better choice since this is a proper probability distribution, so its peak represents the *actual* time when the probability of last scattering was the highest. Nevertheless, if we change these definitions we ought to expect slightly different times as a result.

## 4. Perturbations

The aim of this section is to investigate how small fluctuations in the baryon-photon-dark-matter fluid in the early Universe grew into larger structures. This is done by examining the interplay between the fluctuation of these fluids and the subsequent fluctuations of the space-time geometry, originating from tiny quantum fluctuation in the very early Universe. We will model this by perturbing the flat FLRW-metric using the conformal-Newtonian gauge. This will impact how the Boltzmann equations for the dif-



ferent species behave, from which we are able to construct differential equations for key physical observables, and their initial conditions.

#### 4.1. Theory

We will start by perturbing the flat metric and obtain the terms in the collisionless Boltzmann equation. Next we obtain the collision terms for all relevant species and from this find evolutionary equations for them. We also obtain evolutionary equations for the metric perturbations and express everything in Fourier space, for easier numerical implementation. Lastly we consider the process of inflation, the trick of line of sight integration and some analytical expectations in different regimes.

##### 4.1.1. Metric perturbations

We will consider a perturbed spacetime where we add some contribution,  $h_{\mu\nu}$ , to the flat FLRW metric,  $g_{\mu\nu}^{(0)}$ , of the form:

$$g_{\mu\nu} = g_{\mu\nu}^{(0)} + h_{\mu\nu}. \quad (54)$$

It is fair to assume perturbations to the flat spacetime to be small, so we only concern ourselves with linear perturbations to the metric, which in conformal-Newtonian gauge<sup>13</sup> are:

$$\begin{aligned} h_{00} &= -2\Psi, \\ h_{0i} &= 0, \\ h_{ij} &= 2a^2\delta_{ij}\Phi. \end{aligned} \quad (55)$$

The perturbed metric is (as given in Callin (2006)):

$$g_{\mu\nu} = \begin{pmatrix} -(1+2\Psi) & 0 \\ 0 & e^{2\Phi}\delta_{ij}(1+2\Phi) \end{pmatrix} \quad (56)$$

This means that we perturb the FLRW-metric with  $\Psi \ll 1$  corresponding to the Newtonian potential governing the motion of non-relativistic particles and  $\Phi \ll 1$  governing the perturbation of the spatial curvature.<sup>14</sup> The comoving momentum in this spacetime is:

$$P^\mu = \left[ E(1-\Psi), p^i \frac{1-\Phi}{a} \right]. \quad (57)$$

By considering this momentum, and the geodesic equation in this perturbed spacetime we obtain the following for the time evolution of the spatial coordinates, the directional momentum and the magnitude of the momentum (Dodelson & Schmidt 2020, Eqs. 3.62, 3.69, 3.71):

$$\frac{dx^i}{dt} = \frac{\hat{p}^i}{a} \frac{p}{E} (1 - \Phi + \Psi) \quad (58a)$$

$$\frac{dp^i}{dt} = -\left(H + \frac{d\Phi}{dt}\right)p^i - \frac{E}{a} \frac{\partial\Phi}{\partial x^i} - \frac{1}{a} \frac{p^i}{E} p^k \frac{\partial\Phi}{\partial x^k} + \frac{p^2}{aE} \frac{\partial\Phi}{\partial x^i} \quad (58b)$$

$$\frac{dp}{dt} = -\left(H + \frac{d\Phi}{dt}\right)p - \frac{E}{a} \hat{p}^i \frac{\partial\Psi}{\partial x^i} \quad (58c)$$

<sup>13</sup> This is effectively the coordinate system in which we express the perturbations.

<sup>14</sup>  $\Phi$  may also be interpreted as a *local perturbation to the scale factor*, Dodelson & Schmidt (2020).

Inserting Eq. (58) into Eq. (37), and for now assuming  $C[f] = 0$ , keeping terms to first order only,<sup>15</sup> yield the collisionless Boltzmann equation: (Dodelson & Schmidt 2020, Eq. 3.83):

$$\frac{df}{dt} = \frac{\partial f}{\partial t} + \frac{p}{E} \frac{\hat{p}^i}{a} \frac{\partial f}{\partial x^i} - \left[ H + \frac{d\Phi}{dt} + \frac{E}{ap} \hat{p}^i \frac{\partial\Psi}{\partial x^i} \right] p \frac{\partial f}{\partial p}. \quad (59)$$

Eq. (59) is important as it tells us how the distribution of a species changes in the perturbed spacetime. The remaining work consists mainly of evaluating the collision terms for each species and equate it to Eq. (59) in order to obtain its evolutionary equations. But first, let's take a look at some important mathematical concepts.

##### 4.1.2. Fourier space and multipole expansion

Consider a function  $f(\mathbf{x}, t)$ . Its Fourier transform  $\mathcal{F}$  and inverse  $\mathcal{F}^{-1}$  are defined as:

$$\mathcal{F}[f(\mathbf{x}, t)] \equiv \frac{1}{(2\pi)^{3/2}} \int e^{-i\mathbf{k}\cdot\mathbf{x}} f(\mathbf{x}, t) d^3x = \tilde{f}(\mathbf{k}, t), \quad (60)$$

$$\mathcal{F}^{-1}[\tilde{f}(\mathbf{k}, t)] \equiv \frac{1}{(2\pi)^{3/2}} \int e^{i\mathbf{k}\cdot\mathbf{x}} \tilde{f}(\mathbf{k}, t) d^3k = f(\mathbf{x}, t). \quad (61)$$

It becomes apparent from these definitions that taking the spatial derivative with respect to  $\mathbf{x}$  in real space, is the same as multiplying the function with  $i\mathbf{k}$  in Fourier space. This leads to the following property:  $\mathcal{F}[\nabla f(\mathbf{x}, t)] = i\mathbf{k}\mathcal{F}[f(\mathbf{x}, t)]$ . This is of major significance when working with partial differential equations (PDEs), where:

$$\begin{aligned} \mathcal{F}[\nabla^2 f(\mathbf{x}, t)] &= i^2 \mathbf{k} \cdot \mathbf{k} \mathcal{F}[f(\mathbf{x}, t)] = -k^2 \mathcal{F}[f(\mathbf{x}, t)] \\ \mathcal{F}\left[\frac{d^n f(\mathbf{x}, t)}{dt^n}\right] &= \frac{d^n}{dt^n} \mathcal{F}[f(\mathbf{x}, t)]. \end{aligned} \quad (62)$$

The two equations in Eq. (62) have the ability of reducing PDEs down to a set of decoupled ODEs. This means that we are able to solve for each mode  $k = |\mathbf{k}|$  independently, which will be of great impact for the equations to come.

We will also work with multipole expansions, which are series written as sums of *Legendre polynomials* expanded in  $\mu = \cos\theta \in [-1, 1]$  as:

$$f(\mu) = \sum_{l=0}^{\infty} \frac{2l+1}{i^l} f_l \mathcal{P}_l(\mu), \quad (63)$$

where  $\mathcal{P}_l$  is the  $l$ -th Legendre polynomial. These are orthogonal in such a way that they form a complete basis, enabling us to express any  $f(\mu)$  as in Eq. (63). The coefficients  $f_l$  are the *Legendre multipoles*:

$$f_l = \frac{i^l}{2} \int_{-1}^1 f(\mu) \mathcal{P}_l(\mu) d\mu. \quad (64)$$

The factors  $(2l+1)/i^l$  in Eq. (63) and  $i^l/2$  in Eq. (64) are just conventional choices. It is convenient to expand functions in this way when we are considering quantities that are function of a direction in the sky - since the Legendre polynomials are closely related to the spherical harmonics, which is a natural choice of basis for such quantities.

<sup>15</sup> This is justified by the ansatz that deviations away from the equilibrium distribution of radiation in the inhomogeneous universe are of same order as the spacetime perturbations  $\Phi$  and  $\Psi$ , Dodelson & Schmidt (2020).

#### 4.1.3. Photon perturbation

We have two perturbations to the metric,  $\Phi(\mathbf{x}, t)$  to the spatial curvature, and  $\Psi(\mathbf{x}, t)$  to the Newtonian potential. We seek to find the effect of these perturbations on baryonic matter, dark energy and radiation, as they “live” in a now perturbed spacetime. Let’s start by defining the perturbation to the photons,  $\Theta(\mathbf{x}, \hat{\mathbf{p}}, t)$ , to be the variation of photon temperature around an equilibrium temperature  $T^{(0)}$ :

$$T(\mathbf{x}, \hat{\mathbf{p}}, t) = T^{(0)} [1 + \Theta(\mathbf{x}, \hat{\mathbf{p}}, t)]. \quad (65)$$

This is dependent on the location  $\mathbf{x}$  and the direction of propagation  $\hat{\mathbf{p}}$ , thus capturing both inhomogeneities and anisotropies. We assume  $\Theta$  to be independent of the momentum magnitude.<sup>16</sup> The collision terms for the photons are governed by Compton scattering. We use the form found in (Dodelson & Schmidt 2020, Eq. 5.22):

$$C[f(\mathbf{p})] = -p^2 \frac{\partial f^{(0)}}{\partial p} n_e \sigma_T [\Theta_0 - \Theta(\hat{\mathbf{p}}) + \hat{\mathbf{p}} \cdot \mathbf{v}_b] \quad (66)$$

where  $\Theta_0$  is the monopole term.<sup>17</sup>  $\mathbf{v}_b$  is the bulk velocity of the electrons involved in the process, and is the same as for baryons, hence the subscript. The distribution function for radiation follows the Bose-Einstein distribution function, so we expand  $f$  around its zeroth order Bose-Einstein form, (Dodelson & Schmidt 2020, Eq. 5.2-5.9), using the temperature perturbation in Eq. (65). This is then inserted into Eq. (59), which we equate to the collision term in Eq. (66) in order to obtain the following full Boltzmann equation for radiation:<sup>18</sup>

$$\frac{d\Theta}{dt} + \frac{\hat{p}^i}{a} \frac{\partial \Theta}{\partial x^i} + \frac{d\Phi}{dt} + \frac{\hat{p}^i}{a} \frac{\partial \Psi}{\partial x^i} = n_e \sigma_T [\Theta_0 - \Theta + \hat{\mathbf{p}} \cdot \mathbf{v}_b] \quad (67)$$

#### 4.1.4. Matter perturbation

For massive particles, we start with cold dark matter. Firstly, we assume cold dark matter to not interact with any other species, nor self-interact. Therefore, we do not have any collision terms. Further, we also assume it to behave like a fluid, neglecting any terms not to first order. We consider cold dark matter to be non-relativistic fluid with only a sizeable monopole and dipole term. This fluid description means that the evolution is fully characterised by the density and velocity, (Winther et al. (2023)). We take the first and second moment of Eq. (59) and consider them to first order, in order to retrieve the cosmological generalisation of the continuity equation (Dodelson & Schmidt 2020, Eq. 5.41):

$$\frac{\partial n_c}{\partial t} + \frac{1}{a} \frac{\partial (n_c v_c^i)}{\partial x^i} + 3 \left[ H + \frac{\partial \Phi}{\partial t} \right] n_c = 0, \quad (68)$$

and the Euler equation (Dodelson & Schmidt 2020, Eq. 5.50):

$$\frac{\partial v_c^i}{\partial t} + H v_c^i + \frac{1}{a} \frac{\partial \Psi}{\partial x^i} = 0. \quad (69)$$

<sup>16</sup> This follows from the fact that the magnitude of the photon momentum is virtually unchanged by the dominant form of interaction, Compton scattering (Dodelson & Schmidt (2020)).

<sup>17</sup> This is the integral over the photon perturbation at any given point, over all photon directions. It is given by

$$\Theta_0(\mathbf{x}, t) \equiv \frac{1}{4\pi} \int d\Omega' \Theta(\mathbf{x}, \hat{\mathbf{p}}', t)$$

where  $\Omega'$  is the solid angle spanned by  $\hat{\mathbf{p}}'$  (Dodelson & Schmidt (2020)).

<sup>18</sup> Where of course  $m = 0 \iff E = p$ .

In both Eq. (68) and Eq. (69),  $n_c$  is the cold dark matter number density,  $\mathbf{v}_c$  its bulk velocity. We then consider the perturbation of  $n_c$  to first order:

$$n_c(\mathbf{x}, t) = n_c^{(0)} [1 + \delta_c(\mathbf{x}, t)], \quad (70)$$

and consider the first order perturbation to Eq. (68):

$$\frac{\partial \delta_c}{\partial t} + \frac{1}{a} \frac{\partial v_c^i}{\partial x^i} + 3 \frac{\partial \Phi}{\partial t} = 0. \quad (71)$$

Eq. (71) and Eq. (69) now described the evolution of the density perturbation  $\delta_c$  and bulk velocity  $\mathbf{v}_c$  of cold dark matter.

For baryons (protons and electrons) we also assume them to behave like a non-relativistic fluid, so taking moments is a similar task as for cold dark matter. The only difference is that baryons interact with each other through Coulomb scattering and Compton scattering. We may ignore Compton scattering between protons and photons due to the small cross-section, but electrons are coupled to both photons and protons. Since the first moment of the Boltzmann equation represents conservations of particle number, and none of the above interactions changes the total baryon particle number, the continuity equation is identical to Eq. (68), but for baryons. We also have a baryon perturbation similar to Eq. (70), which altogether results in the following density perturbation for baryons:

$$\frac{\partial \delta_b}{\partial t} + \frac{1}{a} \frac{\partial v_b^i}{\partial x^i} + 3 \frac{\partial \Phi}{\partial t} = 0. \quad (72)$$

For the Euler equation, we now have to consider the collision terms, where momentum is conserved, but transferred between the baryons and photons. This collision term is found from considering the first moment of the photon distribution and find the momentum transfer due to Compton scattering. According to Winther et al. (2023) the momentum transfer in the baryon equation is  $-n_e \sigma_T R^{-1} (v_\gamma^i - v_b^i)$ , where  $R$  is defined in Eq. (48). The Euler equation for baryons, similar to Eq. (69), but with the momentum transfer as source term now yield:

$$\frac{\partial v_b^i}{\partial t} + H v_b^i + \frac{1}{a} \frac{\partial \Psi}{\partial x^i} = -n_e \sigma_T R^{-1} (v_\gamma^i - v_b^i) \quad (73)$$

#### 4.1.5. Evolutionary equations

We have now acquired differential equations for the temperature fluctuations,  $\Theta$  in Eq. (67), and the overdensities<sup>19</sup>,  $\delta_c$ ,  $\delta_b$ , and bulk velocities  $v_c^i$  and  $v_b^i$ , of cold dark matter and baryons respectively in Eq. (71), Eq. (72), Eq. (69) and Eq. (73). In order to make these differential equations easier to solve we make the transformation into Fourier space. We do this by introducing  $\mu$  as the cosine of the angle between the Fourier wave vector  $\mathbf{k}$  and the direction of the photon  $\mathbf{p}/|\mathbf{p}|$ . Additionally, velocities are generally longitudinal which enables us to write:

$$\mu \equiv \frac{\mathbf{k} \cdot \mathbf{p}}{kp} \\ \mathbf{v} = i\hat{\mathbf{k}}v \quad (74)$$

This enables us to summarise the differential equations as follows, now in Fourier space, and the time derivative is with re-

<sup>19</sup> The fluctuations to the equilibrium densities.

spect to conformal time  $\eta$ :

$$\dot{\Theta} = -ik\mu(\Theta + \Psi) - \dot{\Phi} - \dot{\tau} \left[ \Theta_0 - \Theta + i\mu v_b - \frac{\mathcal{P}_2 \Theta_2}{2} \right], \quad (75a)$$

$$\dot{\delta}_c = -3\dot{\Phi} + kv_c, \quad (75b)$$

$$\dot{v}_c = -k\Psi - \mathcal{H}v_c, \quad (75c)$$

$$\dot{\delta}_b = -3\dot{\Phi} + kv_b, \quad (75d)$$

$$\dot{v}_b = -k\Psi + \dot{\tau}R^{-1}(v_b + 3\Theta_1) - \mathcal{H}v_b. \quad (75e)$$

In Eq. (75a) and Eq. (75e) we define  $\dot{\tau}$  from Eq. (44). Additionally, in Eq. (75a) we have included the term  $\mathcal{P}_2 \Theta_2/2$  in order to account for the angular dependency of Compton scattering previously ignored. We have also used that the photon velocity is proportional to the dipole  $\Theta_1 = -v_\gamma/3$ .

Our next step is to once again consider the perturbation to the metric in order to find out how the potentials  $\Psi$  and  $\Phi$  change with time. In short, this is done by computing the perturbed Christoffel symbols using Eq. (56), finding the Ricci tensor and Ricci scalar, and construct the perturbed Einstein tensor. We also have to find the perturbed energy-momentum Tensor, and then solve the Einstein equation in Eq. (1). The result yields the time evolution of  $\Phi$  and  $\Psi$ , where we have from (Dodelson & Schmidt 2020, Eq. 6.41):

$$k^2\Phi + 3\mathcal{H}(\dot{\Phi} - \mathcal{H}\Psi) = 4\pi Ga^2(\rho_c\delta_c + \rho_b\delta_b + 4\rho_\gamma\Theta_0), \quad (76)$$

and from (Dodelson & Schmidt 2020, Eq. 6.47)

$$k^2(\Phi + \Psi) = -32\pi Ga^2(\rho_\gamma\Theta_2) : \quad (77)$$

Eq. (76) and Eq. (77) are both written in Fourier space. The final step is to write the photon fluctuations  $\Theta$  as a hierarchy of multipoles in accordance with Eq. (63). The resultant hierarchy, along with all relevant equations, now written in terms of our preferred temporal variable  $x$  is given below:

### Photon temperature multipoles

$$\Theta'_0 = -\frac{ck}{\mathcal{H}}\Theta_1 - \Phi', \quad (78a)$$

$$\Theta'_1 = \frac{ck}{3\mathcal{H}}\Theta_0 - \frac{2ck}{3\mathcal{H}}\Theta_2 + \frac{ck}{3\mathcal{H}}\Psi + \tau' \left[ \Theta_1 + \frac{1}{3}v_b \right], \quad (78b)$$

$$\Theta'_l = \begin{cases} \frac{lck\Theta_{l-1}}{(2l+1)\mathcal{H}} - \frac{(l+1)ck\Theta_{l+1}}{(2l+1)\mathcal{H}} + \tau' \left[ \Theta_l - \frac{\Theta_2}{10}\delta_{l,2} \right], & l \geq 2 \\ \frac{ck\Theta_{l-1}}{\mathcal{H}} - c\frac{(l+1)\Theta_l}{\mathcal{H}\eta} + \tau'\Theta_l, & l = l_f \end{cases} \quad (78c)$$

### Cold dark matter and baryons

$$\delta'_c = \frac{ck}{\mathcal{H}}v_c - 3\Phi', \quad (79a)$$

$$v'_c = -v_c - \frac{ck}{\mathcal{H}}\Psi, \quad (79b)$$

$$\delta'_b = \frac{ck}{\mathcal{H}}v_b - 3\Phi', \quad (79c)$$

$$v'_b = -v_b - \frac{ck}{\mathcal{H}}\Psi + \tau'R^{-1}(3\Theta_1 + v_b) \quad (79d)$$

### Metric perturbations

$$\Phi' = \Psi - \frac{c^2k^2}{3\mathcal{H}^2}\Phi + \frac{\mathcal{Y}}{2}, \quad (80a)$$

$$\Psi = -\Phi - \frac{12\mathcal{H}^2}{c^2k^2}\Omega_\gamma\Theta_2. \quad (80b)$$

$$\text{where } \mathcal{Y} = \Omega_c\delta_c + \Omega_b\delta_b + 4\Omega_\gamma\Theta_0$$

where we in equation Eq. (78c) truncate the Boltzmann hierarchy by considering the recursion relation of spherical Bessel functions. This ensures that the numerical error of not calculating an infinite number of multipoles does not propagate downwards in order (at least not as fast) and mess up the lower, more important multipoles.

#### 4.1.6. Tight coupling regime

The tight coupling regime represents the time in the early Universe, before recombination, when both radiation, dark matter and baryons were tightly coupled together, interactions where frequent and efficient, and the primordial plasma optically thick ( $\tau \gg 1$ ). Due to this, the bulk velocity of the baryons (which co-moves with the other species due to the tight coupling) is very low. Furthermore, due to the frequent interactions and low bulk velocity the radiation dipole is suppressed. Altogether, this causes the combination  $(3\Theta_1 + v_b)$  to be very small. The optical depth changes rapidly in the tight coupling regime, as seen from Fig. 12,  $|\tau'| \gg 1$ . As a result, any combinations of the form  $\tau'(\Theta_1 + v_b)$ , as they occur in Eq. (78b) and Eq. (79d) are extremely numerically unstable. We therefore use said equations in order to rewrite for:

$$q = \frac{ck}{\mathcal{H}}(\Theta_0 - 2\Theta_2) + \tau'(1 + R^{-1})(3\Theta_1 + v_b) - v_b, \quad (81)$$

where we have defined

$$q \equiv (3\Theta_1 + v_b)' \implies \Theta'_1 = (q - v'_b)/3 \quad (82)$$

We are able to differentiate Eq. (81) w.r.t.  $x$  by using  $(R^{-1})' = -R^{-1}$  in order to obtain:

$$q' = \left[ \tau''(1 + R^{-1}) + (1 - R^{-1})\tau' \right] (3\Theta_1 + v_b) + \left[ \tau'(1 + R^{-1}) - 1 \right] q + \frac{ck}{\mathcal{H}} \left( \Theta_0 - 2\Theta_2 + \Psi + \Theta'_0 - 2\Theta'_2 - \frac{\mathcal{H}'}{\mathcal{H}}(\Theta_0 - 2\Theta_2) \right) \quad (83)$$

The treatment leading up to Eq. (83) is exact, but now we make the following approximation, [Winther et al. \(2023\)](#): In a radiation dominated universe (which is what we have in the tight coupling regime) we have that:

$$\eta \propto a \propto \tau'^{-1} \propto (3\Theta_1 + v_b) \implies \frac{d^2}{d\eta^2}(3\Theta_1 + v_b) \approx 0 \implies q' \approx -\frac{\mathcal{H}'}{\mathcal{H}}q \quad (84)$$

We find  $q$  by equating Eq. (83) and Eq. (84) and solving for  $q$ . We further use Eq. (81) and solve for  $\tau'(1 + R^{-1})(3\Theta_1 + v_b)$  which we substitute into Eq. (79d) in order to obtain an equation for  $v'_b$ . Altogether, this give rise to the following equations, valid in the tight coupling regime:

#### Tight coupling equations

$$q \left[ (1 + R^{-1})\tau' + \frac{\mathcal{H}'}{\mathcal{H}} - 1 \right] = - \left[ \tau''(1 + R^{-1}) + (1 - R^{-1})\tau' \right] (3\Theta_1 + v_b) - \frac{ck}{\mathcal{H}}\Psi + \left( 1 - \frac{\mathcal{H}'}{\mathcal{H}} \right) \frac{ck}{\mathcal{H}}(-\Theta_0 + 2\Theta_2) - \frac{ck}{\mathcal{H}}\Theta'_0 \quad (85)$$

$$v'_b \left[ 1 + R^{-1} \right] = -v_b - \frac{ck}{\mathcal{H}}\Psi + R^{-1} \left( q + \frac{ck}{\mathcal{H}}(-\Theta_0 + 2\Theta_2) - \frac{ck}{\mathcal{H}}\Psi \right) \quad (86)$$

$$\Theta'_1 = \frac{1}{3}(q - v'_b), \quad (87a)$$

$$\Theta_2 = -\frac{20ck}{45\mathcal{H}\tau'}\Theta_1, \quad (87b)$$

$$\Theta_l = -\frac{l}{2l+1} \frac{ck}{\mathcal{H}\tau'}\Theta_{l-1} \quad l > 2. \quad (87c)$$

#### 4.1.7. Modes, scales and the horizon

It is now useful to stop and ponder about what we have achieved so far. We have derived a set of differential equations for the perturbation of cosmological observables. Physically, these perturbations are spatial, but during the derivation we transformed all the equations into Fourier space, whose virtue is to remove the spatial dependency. Instead, the equations are expressed in terms of the *Fourier mode*  $k$ . Each  $k$ -mode is characterised by a co-moving wavenumber  $\mathbf{k}$ , whose angular dependency is contained in the multipole expansion. Thus, we are left with the scalar  $k$  to

represent the original spatial distribution, and indeed; each  $k$  represent a unique *spatial scale*. This is because the Fourier transform decompose the spatial function into its frequency components, and each  $k$  represent a certain frequency, inverse proportional to the wavelength, which represent the physical spatial scale.

Thus, small  $k$ -modes represents large wavelengths which in this context mean perturbations on large scales. On the other hand, large  $k$ -modes represents small-scale perturbations. What is large and what is small is typically defined through the conformal horizon  $\eta$ , as represented in figure Fig. 5, which is a measure of the causally connected regions of the Universe. We follow the definitions of the different regimes as given in [Dodelson & Schmidt \(2020\)](#):

$$\begin{aligned} k\eta &\ll 1 && \text{large scale modes,} \\ k\eta &\simeq 1 && \text{intermediate scale modes,} \\ k\eta &\gg 1 && \text{small scale modes.} \end{aligned} \quad (88)$$

The horizon will evolve in time, and we expect these modes at different scales to also evolve differently in time. At very early times, the horizon is very small, and we expect all modes to be larger than this. We define the concept of *super-horizon* modes, which are modes whose scale is larger than the horizon. We ultimately also have *sub-horizon* modes, where the scale is smaller than the horizon. Different modes are expected to undergo *horizon crossing* at different times.

As a result of this Fourier decomposition, we can investigate what happens at different scales for the various perturbations. In order to re-express the perturbations as function of a physical quantity, say  $\mathbf{x}$ ,<sup>20</sup> we need to integrate across all the different  $k$ -modes, basically accumulating the contributions to the perturbations across all scales.

#### 4.1.8. Inflation

To be able to numerically integrate Eq. (78), Eq. (79) and Eq. (80) we must determine the initial conditions of each quantity. In other words, we need to know how the Universe behaved at a very early stage. It is proposed that an epoch called *inflation* took place, during which the Universe exponentially increased in size during a very short period of time [Dodelson & Schmidt \(2020\)](#).<sup>21</sup> We will describe the inflationary period in order to obtain the initial conditions of the metric perturbations  $\Psi$  and  $\Phi$ .

Assume inflation is driven by a scalar field  $\phi(t, \mathbf{x})$ , typically referred to as *inflaton field*. For inflation to happen, the acceleration of the scale factor must be positive, meaning that the inflaton field must model a fluid where the equation of state parameter  $\omega$  is negative, i.e.  $3p + \rho < 0$ . By considering the temporal and spatial part of the energy-momentum tensor, [Dodelson & Schmidt \(2020\)](#) obtains the following equations for the pressure and density of the inflaton field:

$$\rho_\phi = \frac{1}{2} \left( \frac{d\phi}{dt} \right)^2 + V(\phi), \quad (89)$$

<sup>20</sup> This is the physical spatial variable,  $\mathbf{x}$ , representing a position. If you thought this was a vector quantity of the temporal quantity  $x = \ln a$  you need to evaluate your choices in life.

<sup>21</sup> An inflationary process would also solve the horizon problem, the flatness problem and the monopole problem amongst other things. Details about this can be found in both [Dodelson & Schmidt \(2020\)](#), [Carroll \(2019\)](#), and [Weinberg \(2008\)](#).



and

$$p_\phi = \frac{1}{2} \left( \frac{d\phi}{dt} \right)^2 - V(\phi), \quad (90)$$

where  $1/2 \left( \frac{d\phi}{dt} \right)^2$  is the kinetic energy of the field, and  $V(\phi)$  is the potential energy. Further,  $\omega = p/\rho < 0$  implies that the inflaton field must have more potential than kinetic energy. We therefore require it to *roll slowly* in the potential, and introduce the *slow roll parameters*  $\epsilon_{\text{sr}}$  and  $\delta_{\text{sr}}$ , both of which must be satisfied for the field to be able to perform inflation. These are:

$$\epsilon_{\text{sr}} = \frac{E_{\text{pl}}^2}{16\pi} \left( \frac{V'}{V} \right)^2 \ll 1 \quad (91a)$$

$$\delta_{\text{sr}} = \frac{E_{\text{pl}}}{8\pi} \left( \frac{V''}{V} \right) \ll 1, \quad (91b)$$

where the derivative of the potential  $V$  is in terms of  $\phi$ .

Next, one of the crucial assumptions is that we can express the inflaton field in terms of a perturbation (or overdensity) as:

$$\phi(t, \mathbf{x}) = \phi^{(0)}(t) + \delta\phi(t, \mathbf{x}), \quad (92)$$

where  $\phi^{(0)}$  is the equilibrium value of the field, only dependent on time. We will concern ourselves with the perturbation  $\delta\phi$  and investigate what happens to it during the inflationary period. Before inflation, we expect  $\Psi = \Phi = 0$  and the perturbation  $\delta\phi$  to be of quantum nature.

We could in principle solve the full Einstein equation where  $\Psi$  and  $\Phi$  enters through the Einstein tensor, and  $\phi$  through the energy-momentum tensor.<sup>22</sup> This is not trivial, and instead we introduce the curvature perturbation  $\mathcal{R}(\delta\phi, \Psi)$ , which is a conserved quantity, as [Dodelson & Schmidt \(2020\)](#):

$$\mathcal{R} = -\frac{ik_i \delta T_i^0}{k^2(p + \rho)} - \Psi, \quad (93)$$

where  $k$  is the mode (in Fourier space),  $T_0^i = g^{iv} \partial_v \phi \partial_0 \phi$  is the spatial part of the energy-momentum tensor, and  $p$  and  $\rho$  are the pressure and density.

If we consider the situation before inflation, assume  $\Psi = 0$ . From Eq. (91) we have that  $\rho + p = \dot{\phi}^2/a^2$  using conformal time. Further, according to [\(Dodelson & Schmidt 2020, Eq. 7.47\)](#),  $\delta T_0^i = ik_i \phi \delta\phi/a^3$ . Inserting this into Eq. (93) yield before inflation:

$$\mathcal{R}_{\text{initial}} = -aH \frac{\delta\phi}{\dot{\phi}}. \quad (94)$$

Looking at the same situation at the end of inflation, we now assume radiation domination:  $p = \rho/3$ . According to [Dodelson & Schmidt \(2020\)](#),  $ik_i \delta T_0^i = -4k\rho_\gamma \Theta_1/a$  in the radiation dominated era. Inserting this into Eq. (93) yield:

$$\mathcal{R}_{\text{end}} = -\frac{3aH\Theta_1}{k} - \Psi = -\frac{3}{2}\Psi, \quad (95)$$

where the last equality comes from the postulate that the initial condition for the dipole is  $\Theta_1 = -k\Phi/6aH$ . For the sake of completeness, we now equate Eq. (94) and Eq. (95) to obtain:

$$\Psi = \frac{2}{3} aH \frac{\delta\phi}{\dot{\phi}} \Big|_{\text{horizon crossing}}, \quad (96)$$

which is the value of  $\Psi$  immediately after inflation, when the mode is of equal size as the horizon (hence horizon crossing).

#### 4.1.9. Initial conditions

We now seek to determine the actual initial conditions enabling us to solve the desired differential equations. At very early times, we make the following assumptions:

$$k\eta \ll 1 \iff \frac{k}{\mathcal{H}} \ll 1 \quad (97a)$$

$$\tau \gg 1 \text{ and } |\tau'| \gg 1 \quad (97b)$$

$$\Theta_0 \gg \Theta_1 \gg \Theta_2 \gg \dots \gg \Theta_l. \quad (97c)$$

Eq. (97a) is necessary in order to ensure causally disconnected regions in the early universe. It also ensures that the modes we are interested in today is outside the horizon [Winther et al. \(2023\)](#). We have already established that the universe is optically thick, so Eq. (97b) follow directly from Fig. 12. Further, at these scales we expect the lower multipoles to be dominant, thus Eq. (97c) holds. This is because the causal horizon is smaller than the  $k$ -modes, making the radiation observed by an hypothetical observer nearly uniform. Applying the assumptions in Eq. (97) to Eq. (78), Eq. (79) and Eq. (80) allows to determine the initial conditions.

Firstly, the perturbations of  $\Phi$  and  $\Psi$  evolves slowly outside the horizon, so we may approximate  $\Phi' = \Psi' = 0$ . However, we will use their expressions in order to determine other initial conditions. In the following we make use of the assumptions in Eq. (97). Eq. (78a) becomes  $\Theta'_0 = -\Phi'$ . Further, Eq. (80a) turn into  $\Phi' = \Psi + 2\Theta_0 \implies \Theta_0 = -\Psi/2$ . The overdensities Eq. (79c) and Eq. (79a) have similar behaviour<sup>23</sup> and we write  $\delta' = -3\Phi' = 3\Theta'_0$ . Integrating both sides yield  $\delta = -3\Psi/2 + C$ , where  $C$  is the integration constant. This is put to zero, making the initial conditions *adiabatic*. Eq. (80b) now fixes the relation between the initial conditions of  $\Psi$  and  $\Phi$  as  $\Phi = -\Psi$ .

For the velocities, we expect the baryon and cold dark matter velocities to have the same initial value, and we find it by considering Eq. (79b), which can be written as  $(va)' = -cka\Psi/\mathcal{H}$ . Integration yields  $v = -ck\Psi/2\mathcal{H}$  where we have omitted the constant of integration. We find the initial conditions for the next multipole terms by following a similar logic. This is also shown in [\(Dodelson & Schmidt 2020, Eq. 7.59\)](#) which fixes the velocities as  $v = 3ck\Phi/6\mathcal{H}$ ,<sup>24</sup> and gives the initial dipole moment  $\Theta_1 = -k\Phi/6aH$ . Inserting this into Eq. (95) yields the desired  $\mathcal{R} = -2\Psi/2$ . Since  $\mathcal{R}$  is conserved, choosing a value for it equates to fixing a normalisation. We will simply use  $\mathcal{R} = 1$ . The full set of adiabatic initial conditions then become:

<sup>23</sup> Because gravity does not care whether it acts on baryons or dark matter.

<sup>24</sup> [Dodelson & Schmidt \(2020\)](#) uses  $iv$  as velocities, but we have multiplied the velocities with  $i$  in order to make them real, but ultimately changing signs.

<sup>22</sup> The energy-momentum tensor for  $\phi$  is given in [\(Dodelson & Schmidt 2020, Eq. 7.6\)](#) as:

$$T^\alpha_\beta = g^{\alpha\nu} \frac{\partial\phi}{\partial x^\nu} \frac{\partial\phi}{\partial x^\beta} - \delta^\alpha_\beta \left[ \frac{1}{2} g^{\mu\nu} \frac{\partial\phi}{\partial x^\mu} \frac{\partial\phi}{\partial x^\nu} + V(\phi) \right].$$



### Initial conditions

$$\Psi = -\frac{2}{3}, \quad (98a)$$

$$\Phi = -\Psi, \quad (98b)$$

$$\delta_c = \delta_b = -\frac{3}{2}\Psi, \quad (98c)$$

$$v_c = v_b = -\frac{ck}{2\mathcal{H}}\Psi, \quad (98d)$$

$$\Theta_0 = -\frac{1}{2}\Psi, \quad (98e)$$

$$\Theta_1 = \frac{ck}{6\mathcal{H}}\Psi, \quad (98f)$$

$$\Theta_2 = -\frac{20ck}{45\mathcal{H}\tau'}\Theta_1, \quad (98g)$$

$$\Theta_l = -\frac{l}{2l+1}\frac{ck}{\mathcal{H}\tau'}\Theta_{l-1}. \quad (98h)$$

#### 4.1.10. Line of sight integration

We are in principle able to solve for any  $\Theta_l$ , but it has to be done iteratively. This is very computationally expensive, so much so that it is desirable to obtain a method of finding *any*  $\Theta_l$  independently. Thankfully, this is possible and obtained through a method called *line of sight integration*. The idea behind the line of sight integration was first proposed by [Seljak & Zaldarriaga \(1996\)](#), where instead of expanding the photon perturbation in multipoles and then integrating, the integral is solved explicitly and expanded into multipoles at the end. The gist of the derivation is to start with Eq. (75a) and rewrite it into a form:  $\dot{\Theta} + (ik\eta - \dot{\tau}) = S$ , where  $S$  is for now just a source term.<sup>25</sup> This can be rewritten into:

$$e^{-ik\mu\eta+\tau} \frac{d}{d\eta} [\Theta e^{ik\mu\eta-\tau}] = S, \quad (99)$$

which we can integrate by parts to obtain:

$$\Theta(k, \mu, \eta_0) = \int_{\eta_i}^{\eta_0} S e^{ik\mu(\eta-\eta_0)-\tau} d\eta, \quad (100)$$

where  $\eta_0$  is the conformal time today and  $\eta_i$  is the initial time from which we start integrating. Eq. (100) tells us physically that in order to obtain the photon perturbation today, we can integrate an exponentially attenuated source term along the past light cone of the photon.<sup>26</sup> Then, following the discussion in ([Dodelson & Schmidt 2020](#), Eq. 9.49 - Eq. 9.54) we are able to decompose Eq. (100) into its individual multipoles, now expressed in terms of  $x$ :

$$\Theta_l(k, x=0) = \int_{-\infty}^0 S(k, x) j_l[k(\eta_0 - \eta(x))] dx, \quad (101)$$

where  $j_l[k(\eta_0 - \eta(x))]$  are the spherical Bessel functions which account for the projection of some three-dimensional signal<sup>27</sup>

onto a two-dimensional sphere.<sup>28</sup>  $S(k, x)$  is known as the *source function* and is given by:

$$\begin{aligned} S(k, x) = & \tilde{g} \left[ \Theta_0 + \Psi + \frac{\Theta_2}{4} \right] & (\text{SW}) \\ & + e^{-\tau} [\Psi' - \Phi'] & (\text{ISW}) \\ & - \frac{1}{ck} \frac{d}{dx} [\mathcal{H} \tilde{g} v_b] & (\text{Doppler}) \\ & + \frac{3}{4c^2 k^2} \frac{d}{dx} \left[ \mathcal{H} \frac{d}{dx} (\mathcal{H} \tilde{g} \Theta_2) \right] & (\text{Polarisation}). \end{aligned} \quad (102)$$

We can thus find any multipole  $\Theta_l$  simply by knowing  $\Theta_0, \Theta_1, \Theta_2, \Psi, \Phi, v_b$  and their derivatives, which is rather remarkable. The physical interpretation of the line of sight integral is that we “look back” through time and consider the various physical effects affecting the evolution of the photon multipoles. The first of which is the *Sachs-Wolfe* effect (SW), which is the main contributor. The term in the bracket is an effective photon temperature,<sup>29</sup> where the  $\Theta_2$  represent a small quadrupole correction. We know this is small as the whole bracket is weighted by the visibility function which peaks during recombination, where the main contributors are the monopole and dipole. Thus, the main contributor to the anisotropies we observe today are the inhomogeneities in photon temperature present at the time of recombination [Winther et al. \(2023\)](#).

The remaining terms in Eq. (102) are corrective effects that the photons undergo as they free stream from the last scattering surface at recombination until today. The second term is the *integrated Sachs-Wolfe* effect which describe the energy change of photons as they pass through potential wells that *vary in time*. The third term contains the baryon bulk velocity  $v_b$  and thus describe a Doppler shift, either of moving observers or moving sources. The fourth term is mainly due to polarisation, like Thomson scattering or gravitational lensing by large structures. However, since we ignore polarisation here, the corrections of this term comes from the quadrupole, but we still call it the polarisation term.

Due to the nature of the product rule, Eq. (102) end up containing a lot of terms. We state the individual result of the differentiated terms below:

$$\frac{d}{dx} [\mathcal{H} \tilde{g} v_b] = \mathcal{H} \tilde{g}' v_b + \mathcal{H} \tilde{g} v_b' + \mathcal{H}' \tilde{g} v_b \quad (103)$$

and

$$\begin{aligned} \frac{d}{dx} \left[ \mathcal{H} \frac{d}{dx} (\mathcal{H} \tilde{g} \Theta_2) \right] = & \tilde{g} \Theta_2 [\mathcal{H}'' \mathcal{H} + (\mathcal{H}')^2] \\ & + \mathcal{H}^2 [\tilde{g} \Theta_2'' + \tilde{g}'' \Theta_2 + 2\tilde{g}' \Theta_2'] \\ & + 3\mathcal{H}' \mathcal{H} [\tilde{g} \Theta_2' + \tilde{g}' \Theta_2]. \end{aligned} \quad (104)$$

In order to find  $\Theta_2'$  we insert  $l = 2$  in Eq. (78c) and differentiate:

$$\begin{aligned} \Theta_2'' = & \frac{d}{dx} \left[ \frac{2ck}{5\mathcal{H}} \Theta_1 - \frac{3ck}{5\mathcal{H}} \Theta_3 + \tau' \left( \Theta_2 - \frac{\Theta_2}{10} \right) \right] \\ = & \frac{2ck}{\mathcal{H}} \left( \Theta_1' - \frac{\mathcal{H}'}{\mathcal{H}} \Theta_1 \right) + \frac{3ck}{5\mathcal{H}} \left( \frac{\mathcal{H}'}{\mathcal{H}} \Theta_3 - \Theta_3' \right) \\ & + \frac{9}{10} (\tau'' \Theta_2 + \tau' \Theta_2') \end{aligned} \quad (105)$$

<sup>25</sup> Will return to this later, as the source function  $S$ , which serves as the source term when using our preferred coordinate  $x$  in Fourier space.

<sup>26</sup> Hence the name: line of sight integration.

<sup>27</sup> Characterised by  $l$ .

<sup>28</sup> Characterised by  $l$ .

<sup>29</sup> Described mainly by the monopole term, and the change in frequency of photons induced as gravitational redshift by  $\Psi$ .

Thus, by calculating  $\Theta_0$ ,  $\Theta_1$  and  $\Theta_2$  (plus their derivatives)<sup>30</sup> iteratively, we are able to independently find any  $\Theta_l$  by integrating the source function (multiplied by the spherical Bessel functions) along the past light cone of a photon.

#### 4.1.11. Analytical expectations

Let's start by considering large scale modes. These will enter the horizon at late times, and thus experience the transition from radiation to matter domination before horizon-crossing. We are able to find an analytical approximation for the potential  $\Phi$  in the large scale super-horizon regime that will be valid for the transition from radiation to matter domination. This solution is (Dodelson & Schmidt 2020, Eq. 8.31):

$$\Phi(\mathbf{k}, y) = \frac{1}{10y^3} \left[ 16\sqrt{1+y} + 9y^3 + 2y^2 - 8y - 16 \right] \Phi(\mathbf{k}, 0), \quad (106)$$

where we define the new variable  $\ln y \equiv x - x_{\text{RM}}$ . We see that even for the large scales, that enter the horizon at really late times, the potential will decrease by 9/10 during the transition from radiation to matter domination.<sup>31</sup> Further, Dodelson & Schmidt (2020) claim that the potential will remain constant during matter domination. In other words, it will not change when it enters the horizon since the expansion of the Universe in a matter dominated universe balances the accretion of matter in potential wells. When the universe starts to expand more rapidly during dark energy domination, the accretion of matter will be overpowered by the expansion rate and thus the potentials will decay during this period.

There are also analytical approximations to the small scale modes. Firstly, for the potential during radiation domination we have (Dodelson & Schmidt 2020, Eq. 8.46):

$$\Phi(\mathbf{k}, \eta) = 2 \left( \frac{\sin r - r \cos r}{r^3} \right)_{r=k\eta/\sqrt{3}} \mathcal{R}(\mathbf{k}), \quad (107)$$

which assumes a constant initial condition which is fair since initially all modes are outside the horizon, unaffected by causal physics. What we draw from this is that if the mode enters the horizon during radiation domination it can be approximated by Eq. (107) and experience oscillations and decay.

For completeness we also state the *Meszaros equation* governing evolution of dark matter perturbations on sub-horizon scales (Dodelson & Schmidt 2020, Eq. 8.59):

$$\frac{d^2 \delta_c}{dy^2} + \frac{2+3y}{2y(y+1)} \frac{d\delta_c}{dy} - \frac{3}{2y(y+1)} \delta_c = 0. \quad (108)$$

Analytical solutions to the dark matter perturbations in this regime are non-trivial as Eq. (108) require radiation perturbation to be negligible. In short, according to Dodelson & Schmidt (2020), the cold dark matter perturbations will be constant for super-horizon scales, grow logarithmically after horizon crossing, while still in the radiation domination regime, and grow with the scale factor according to Eq. (108) during matter domination.

The last analytical expression we consider is the analytical approximation of the equation of motion of the photon monopole

(Dodelson & Schmidt 2020, Eq. 9.20):

$$\begin{aligned} \Theta_0'' + \frac{a'}{a} \frac{R}{1+R} \Theta_0' + k^2 c_s^2 \Theta_0 &= F(k, \eta) \\ F(k, \eta) &\equiv -\frac{k^2}{3} \Psi - \frac{a'}{a} \frac{R}{1+R} \Phi' - \Phi'', \end{aligned} \quad (109)$$

which describes oscillations with a drag component proportional to  $\Theta_0'$  (second component on the left of the top equation) and force term  $F$ . The homogeneous solutions to Eq. (109) are sines and cosines of the argument  $kr_s$  where  $r_s$  is the sound horizon. Thus, the physical solution are sound waves propagating at the speed of sound  $c_s$ , constantly defining the sound horizon.

#### 4.2. Methods

It is now time to find solutions to the equations we have developed. The first task is to determine when we have to use the tight coupling equations in Eq. (85), Eq. (86) and Eq. (87). As discussed in Section 4.1.6, the tight coupling regime should be used for early times, when  $\tau, |\tau'| \gg 1$ . We expect it to last no longer than until recombination, and thus define a higher threshold of  $x = -8.3$ . We also have from Callin (2006) that  $ck/(\mathcal{H}\tau') \ll 1$  during tight coupling. Therefore, we adopt the following conditions, all of which must be satisfied for the tight coupling regime to be valid:

$$\begin{aligned} \left| \frac{d\tau}{dx} \right| &= \tau' > 10 \\ \left| \frac{d\tau}{dx} \right| &= \tau' > \frac{10ck}{\mathcal{H}} \\ x &< -8.3 \end{aligned} \quad (110)$$

As soon as one of the above conditions fails, we must adopt the full system described in Eq. (78), Eq. (79) and Eq. (80). It is therefore wise to implement a routine that finds  $x = x_{\text{tc}}$  which will be the transition between tight coupling and the full system. This value will change with  $k$ .

When integrating we use uniformly spaced values of  $x \in [-20, 0]$  and logarithmically spaced values of  $k \in [0.00005, 0.3]/\text{Mpc}$ . The differential equations are then solved with the initial conditions from Eq. (98) for  $x \in [-20, x_{\text{tc}}]$ . After tight coupling, the differential equations are solved with initial conditions given as the last solution of the tight coupling equations, for  $x \in (x_{\text{tc}}, 0]$ . At the end, both solutions (for all  $k$ -s) are “sown” together using the same  $x$ -array, and splined for all  $x$  and  $k$ .

When finding the source function we use the same  $x$  and  $k$  arrays as in the section above, and solve Eq. (102) for each combination. The result is then splined.

When analysing the results, we choose  $k$ -modes from all the regimes described in Section 4.1.7:  $k_1 = 0.001/\text{Mpc}$  as the large scale mode,  $k_2 = 0.01/\text{Mpc}$  as the intermediate scale mode and  $k_3 = 0.1/\text{Mpc}$  as the small scale mode.

#### 4.3. Results and discussion

We present the results of the numerical solutions of the Einstein-Boltzmann equations and discuss them in due order starting with the potentials, then the multipoles and finally the matter perturbations. The main focus is on the evolution of these perturbations, leaving the discussion of the initial conditions for the next section.

<sup>30</sup> Also  $\Theta_3$  and  $\Theta_3'$  if we want to solve  $\Theta_2'$  analytically.

<sup>31</sup> Since  $x \gg x_{\text{eq}} \implies y \gg 1$

#### 4.3.1. Potentials

Fig. 14 shows the metric perturbation potentials  $\Phi$  and  $\Psi$  as functions of time  $x$  for the  $k$ -modes under investigation. The time of matter-radiation equality and recombination is marked in the plot as black dash-dotted and a shaded grey area respectively. Let's first consider the top panel, showing only  $\Phi$ . At early times, it is constant across all  $k$ -modes.<sup>32</sup> This is expected since at early times, the horizon is small and most modes are larger than this. Thus, they will be unaffected by causal physics and stay constant at their initial value. As time proceeds, the smaller  $k$ -modes will enter the horizon and are suddenly subjected to causal physics. We see from the top panel that if this happens in the radiation dominated regime (before radiation-matter equality), the potential will decline as  $e^{-2x}$ . This can be seen from Eq. (80a). In addition, the damped oscillations predicted by Eq. (107) are clearly seen for these scales. The smaller the scale, the earlier it crosses the horizon, and the more suppression, oscillation and damping it experiences. In order to explain the physics behind this we must consider the primordial baryon-photon plasma which exert a radiation pressure, which is the dominant component of the universe at this time (hence radiation domination). This pressure counteracts gravitational forces and will prevent overdensities of the photon-baryon fluid from growing, effectively making the potential decay as a result of an expanding universe. The main source of the potential in the radiation era is thus the dark energy, of which we have a constant amount that does not couple to photons nor baryons. Therefore, if the universe expands as  $\sim a^2 = e^{2x}$ ,<sup>33</sup> the potential must decay as the inverse. As this decay happens, the potential will experience oscillations due to the interplay between accretion of baryons in gravitational wells, and the counter-acting radiation pressure.

However, for large scale modes, like the blue graph, where horizon crossing happens in the matter dominated regimes, then we expect the potential to change with a factor 9/10 as it transitions from radiation domination to matter domination, from Eq. (106). If modes cross the horizon during matter domination then the potential stays constant. This is because the expansion factor of the universe during matter domination balances the accretion of matter in overdense regions. This is further emphasised after recombination when baryons decouple from photons and evolve with dark matter instead, not being subjected to the radiation pressure.

The sum of the potentials in the bottom panel of Fig. 14 goes as  $\Psi + \Phi \sim e^{-2x}/k^2\Theta_2$ , so it will closely follow the quadrupole term, but being suppressed by an exponential factor. Also, the  $k^2$  term suggested larger value for small  $k$ -s (large scale). We save the discussion of the quadrupole, but the latter can clearly be seen as the large and intermediate scale modes show sinusoidal behaviour, with the large scale mode having a larger amplitude. Both are exponentially suppressed. These effects happen when the tight coupling epoch is over, since all multipoles except the monopole and dipole are suppressed during tight coupling.

#### 4.3.2. Multipoles

We now focus our attention on the multipoles, starting with the monopole term expressed through the photon overdensity  $\delta_\gamma = 4\Theta_0$ . Mathematically, this relation can be seen from either the parenthesis in Eq. (76) or the definition of  $\mathcal{Y}$  in Eq. (80)

<sup>32</sup> When referring to “all  $k$ -modes” it is implicit that we only mean the three modes considered here, but the qualitative discussions should be valid across all  $k$ -modes.

<sup>33</sup> Valid in the radiation dominated era since  $a(t) \propto t^{1/2}$  in this regime.

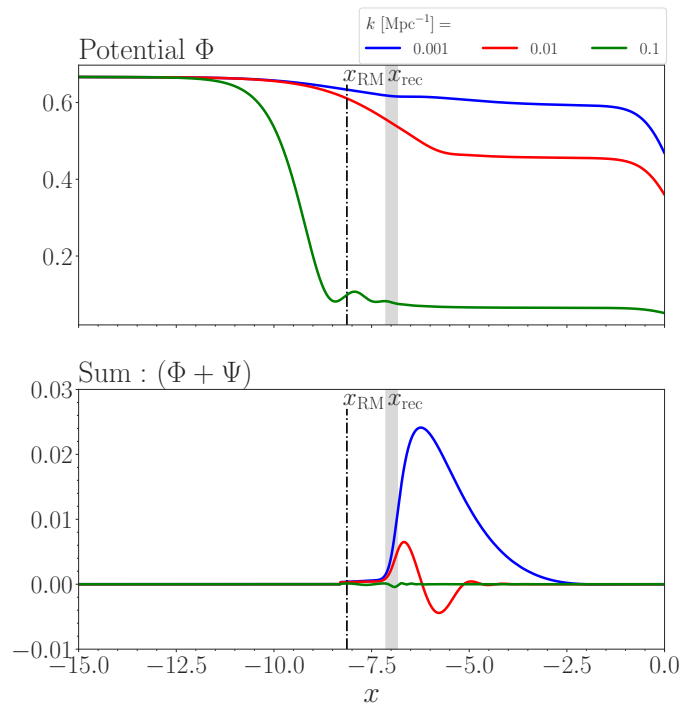


**Fig. 14.** The metric perturbation potentials,  $\Psi$  representing the Newtonian potential, and  $\Phi$  representing the spatial curvature perturbation. Both panels show the evolution as function of the time  $x$ , for the three different  $k$ -modes outlined in Section 4.2. The top panel shows  $\Phi$  alone, while the bottom shows the sum of the two. The grey shaded are represent the time of recombination as found in Section 3, highlighting the fact that it did not occur in an instant, and the dash-dotted black line is the time of radiation-matter equality as found in Section 2.

following somewhat diffuse symmetry arguments. Physically it also makes sense since the photon monopole is some measure of the average photon temperature which intuitively can be thought of as a photon overdensity. It can be seen for the various  $k$ -modes in Fig. 15, where we clearly see that the small scale perturbation undergoes horizon crossing first, and become subject to causal physics. This is manifest in the oscillation of the green curve in the figure. Metric perturbations and pressure will generate acoustic oscillations within causally connected regions. When the horizon increases, these oscillations will affect a spatially large area, affecting  $k$ -modes on larger and larger scales. This is also manifest in Fig. 15 as the intermediate  $k$ -mode starts to oscillate later, and finally the large scale mode.

What are the monopole fluctuations really? The different modes represent the average temperature at different physical length scales. At early times, when the horizon is small, most modes are outside it, leaving their average temperature and thus monopole constant. As modes enter the horizon, they become subject to causal physics, like the gravitational potential. Since photons and baryons are coupled at early times, photons must continuously climb in and out of the gravitational potential wells set up by matter, gaining and losing energy in the process. It is worth noticing that this manifest itself as oscillations in Fourier space, but can be interpreted as propagating acoustic waves in real space. Before recombination, for modes having entered the horizon, these are waves in the baryon-photon fluid, propagating with the speed of sound. The origin of these oscillations in the radiation era is the decay of the gravitational potentials (discussed in the previous section), an effect called *radiation driving*, which we may interpret to be included in the force term in Eq. (109).

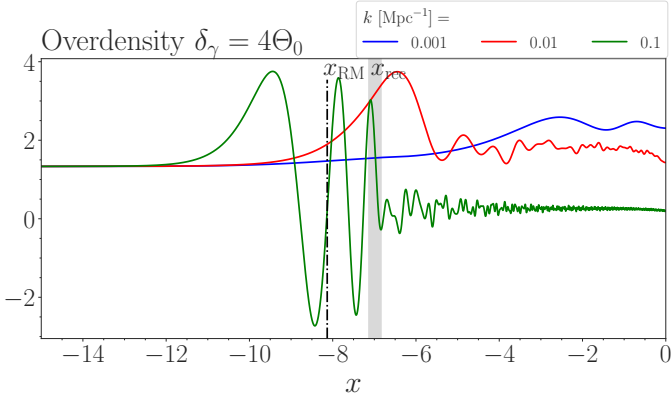


**Fig. 15.** Photon overdensity represented by the photon monopole for the various  $k$ -modes. Recombination is marked as a shaded grey area. The time of radiation-matter equality is marked with a dashed black line.

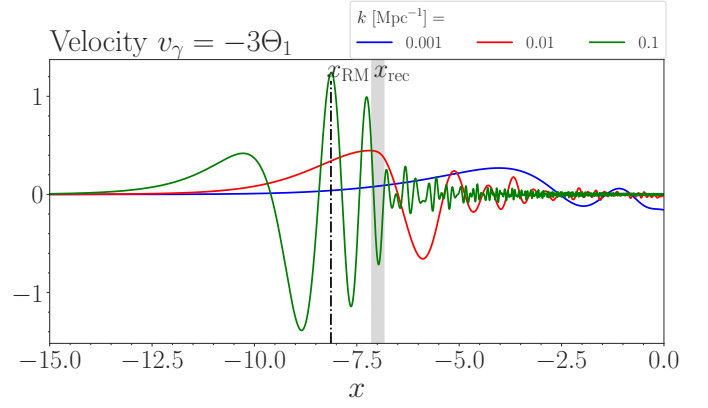


**Fig. 16.** Photon velocity represented by the photon dipole for the various  $k$ -modes. Recombination is marked as a shaded grey area. The time of radiation-matter equality is marked with a dashed black line.

The oscillations are also asymmetric about its equilibrium position. This is due to *baryon loading* where the potentials change slightly because of the oscillating baryons, whereas the radiation pressure is left unchanged. The fact that the baryons and photons move together affects the sound speed which also causes some asymmetry to the oscillations. After recombination, photons decouple from baryons and stream freely throughout the Universe. During this decoupling process the interaction rate between photons and baryons decreases, but does not become zero. There are still interactions, causing energy to be transported and, temperature fluctuations on small scales to become washed out. This is known as diffusion damping, and smooths out the small scale perturbation for both radiation and matter. This is manifest for the small scale mode in green in Fig. 15 as its amplitude decays after recombination. This phenomenon is not present for the modes entering the horizon after decoupling, in the matter regime.

Thus, the photon monopole perturbation behaves somewhat according to Eq. (109), where the oscillations are sourced by some force term (mainly radiation driving and baryon loading) which is a function of the potentials. This is true before decoupling for modes having entered the horizon. Super-horizon modes hardly evolve at all, due to the lack of causal physics at these scales.

A similar discussion to the one above can be applied on the photon velocity  $v_\gamma = -3\Theta_1$ , as shown in Fig. 16. Similarly to the monopole, small scale modes enter the horizon first and start to oscillate followed by larger scale modes. Modes entering the horizon before recombination experience diffusion damping, effectively smoothing the average velocity of the photons. Worth noticing in this plot is that for similar modes, the oscillatory behaviour of the photon velocity is starting slightly before the overdensity. This makes sense, since we need something to be moving in the first place for overdensities to occur.

The same is the case for the quadrupole in Fig. 17. However, as previously assumed, the quadrupole term is strongly suppressed during tight coupling, but behave similarly to the lower order multipoles after tight coupling. This is because during tight coupling, the photon-baryon plasma behaved very much like a fluid, only described by some average temperature and a velocity. Hence, there were no significant quadrupole (or any higher order multipole) moment(s) in this regime. Considering the large and intermediate scale modes (blue and red curve) we are able to close the discussion of the sum of potential in Fig. 14, where the quadrupole was the main contributor to the sinusoidal fre-

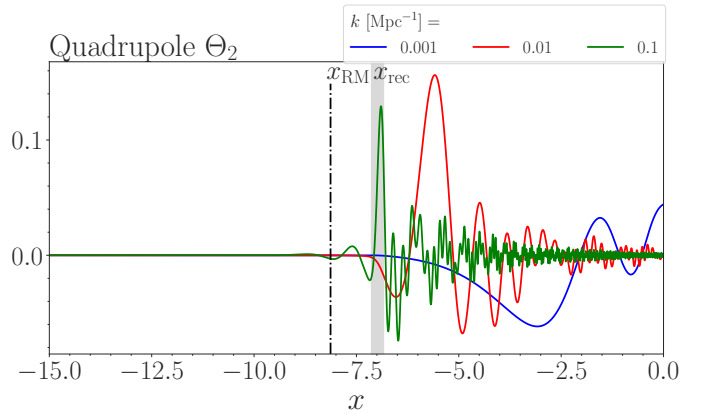


**Fig. 17.** Quadrupole term of the photon perturbation. This term only becomes relevant after tight coupling. Recombination is marked as a shaded grey area. The time of radiation-matter equality is marked with a dashed black line.

quency, and  $k$  to the amplitude. The small scale modes of the quadrupole experience the same diffusion damping as the lower multipoles.

#### 4.3.3. Matter perturbations

Fig. 18 show the overdensities of cold dark matter and baryons as function of time  $x$ , for the various  $k$ -modes. The small scale mode (green) enter the horizon during radiation domination, and immediately begins to cluster in overdense regions. The cold dark matter is not coupled to anything so its overdensity evolves on its own, only restricted by the growth of the Universe itself. During radiation domination, the rapid expansion of the Universe makes the evolution of the cold dark matter logarithmic. Baryons, on the other hand, are coupled to photons and experiences photon radiation pressure which prevent their overdensities from growing. Instead, the interplay between radiation pressure and gravitation propagate acoustic sound waves in the plasma, manifest as oscillations in Fourier space. These are seen in the plot (green dashed line). These oscillations will continue as long as photons and baryons are coupled. As we transition from radiation to matter domination, the evolution of the dark matter overdensity change from a logarithmic relationship to a power law scaling with the scale factor  $a$ . This is because the expansion rate of the Universe change alongside its dominant con-



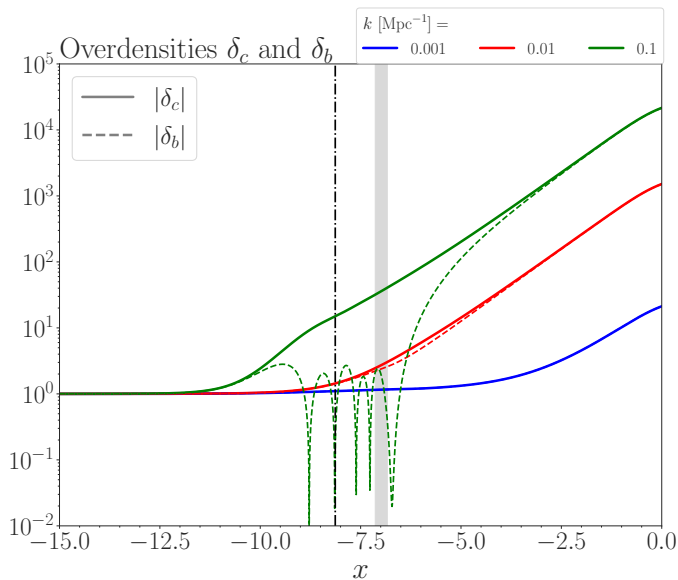


**Fig. 18.** The overdensities of cold dark matter and baryons for the various  $k$ -modes. Recombination is marked as a shaded grey area. The time of radiation-matter equality is marked with a dashed black line.

stituent, and when matter becomes dominant, the expansion rate decreases. This enables larger perturbations in the dark matter. The behaviour of the baryons change once they decouple from the photons. Now they do not feel the same radiation pressure as before, so they start to gather in the potential already in existence due to dark matter. This happens slightly after decoupling. There is a small delay due to Compton drag, photons diffuse and scatter of baryons, and the baryons already have some velocity from the oscillation.<sup>34</sup> From now on, the baryons fall into the gravitational wells, and all matter evolve together deep in matter domination. Close to  $x = 0$ , when dark energy become the dominant constituent, the acceleration of the universe increases and the matter overdensities grow slower because of this.

The intermediate scale mode enters the horizon around the time of radiation matter equality, so the baryons deviate slightly from the dark matter evolution. However, there is not any oscillatory behaviour since this mode did not enter the horizon early enough to capture the oscillations of the plasma. During matter domination, all matter evolves similarly; growing as a power law w.r.t. the scale factor. The blue line representing large scale modes show this, entering the horizon deep in matter domination and immediately starts to grow according to this power law.

We emphasise the above discussion by considering only the small scale mode, and including the photon overdensity as well. This is shown in Fig. 19. We recognise the dark matter and baryon overdensities, and we also clearly see the coupling between baryons and photons at early times, before recombination. After this, the baryon evolves as the dark matter while the photons diffuse, reducing the amplitude of their oscillations, effectively smoothing their overdensities. This diffusion drags out the time it takes for the baryons to fall in to the potentials (to keep up with dark matter). This is the effect of Compton drag, as diffusion is effectively photons interacting with electrons through Compton scattering, with an increased mean free path between each interaction.

<sup>34</sup> The width of the grey shaded area showing recombination cannot be taken literally as it is there just to showcase the fact that recombination and decoupling are not instantaneous processes.

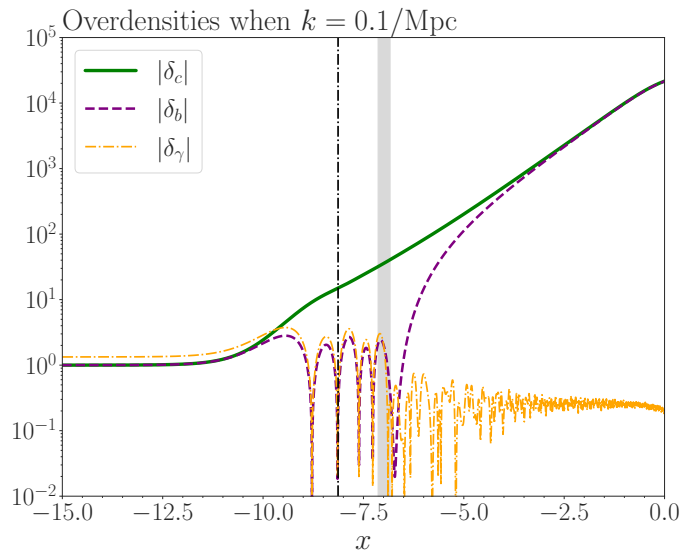


**Fig. 19.** Comparison of the overdensities of cold dark matter, baryons and photons for a small scale mode. We clearly see the decoupling of photons from baryons during recombination, which is marked as a shaded grey area. The time of radiation-matter equality is marked with a dashed black line.

Fig. 20 show the velocities (bulk velocity of the fluid motion) of the cold dark matter and baryons. We start by noticing that for super-horizon scales (to the left of the plot), the velocities are the same for baryons and cold dark matter, and it follows the expansion of the Universe. It must be so, because no physics can affect the velocity which must be comoving as the Universe expands. For scales entering the horizon at late times it is always like this (blue line); the velocity follows the expansion of the Universe since the physical overdensity is in the same comoving location (for large scales). For baryons entering the horizon during radiation domination (small scales) it is a different story as this is an acoustic wave travelling outwards with some velocity. This is captured as oscillations in Fig. 20. The cold dark matter overdensities for small scales will also have a bulk velocity relative to the comoving coordinate system as these overdensities are subjected to the changing potentials. Fig. 21 compares the bulk velocities of cold dark matter, baryons and photons for a small scale mode. Once again we notice the decoupling of the photons after recombinations. This plots tells pretty much a similar story as Fig. 19.

## 5. Power spectra

In this section we will construct the angular power spectrum and the matter power spectrum in order to compare our theoretical predictions with actual observables.

### 5.1. Theory

Before delving into the theory of power spectra we must make one distinction clear: When we studied the evolution of the temperature perturbation  $\Theta$  in Section 4.1 we divided the evolution into two stages, namely the initial value of the perturbation, set up by inflation, and the evolution in time. We are able to treat them separately since we only consider perturbations to first order. We had that the initial perturbations were caused by the curvature perturbation  $\mathcal{R}$ . The evolution from initial perturbations to observable anisotropies is called the *transfer function* and is



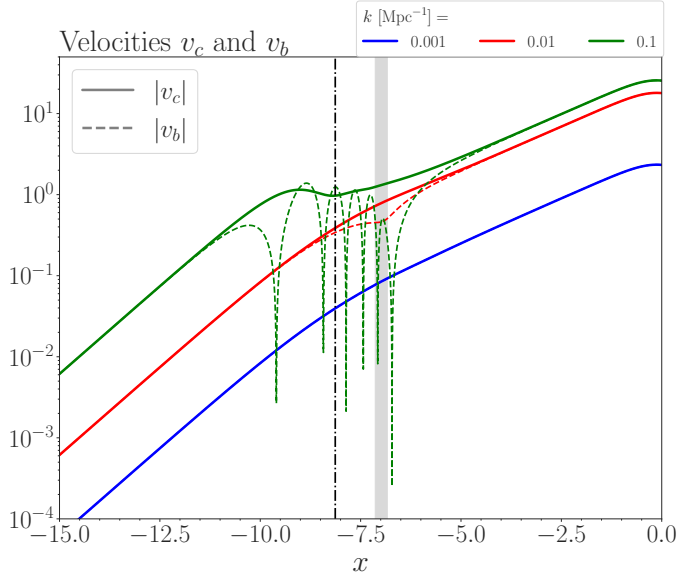


**Fig. 20.** The bulk velocities of cold dark matter and baryons for the various  $k$ -modes. Recombination is marked as a shaded grey area. The time of radiation-matter equality is marked with a dashed black line.

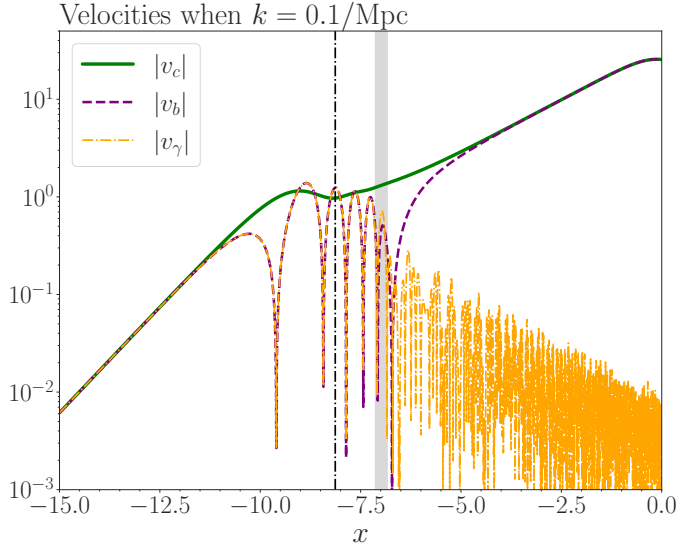


**Fig. 21.** Comparison of the bulk velocities of cold dark matter, baryons and photons for a small scale mode. We clearly see the decoupling of photons from baryons during recombination, which is marked as a shaded grey area. The time of radiation-matter equality is marked with a dashed black line.

the quantity,  $\Theta$ , for which we have already developed equations of motion, and will be solved for in our code. When solving we simply put  $\mathcal{R} = 1$ ,<sup>35</sup> but if we want to compare our results to actual observables we need to include the initial perturbations. Thus:

$$\Theta_l^{\text{Obs}}(\mathbf{k}, t) = \Theta_l(k, t)\mathcal{R}(\mathbf{k}) \iff \Theta_l(k, t) = \frac{\Theta_l^{\text{Obs}}(\mathbf{k}, t)}{\mathcal{R}(\mathbf{k})}. \quad (111)$$

$\Theta$  is referred to as  $\mathcal{T}$  (transfer function) in Dodelson & Schmidt (2020).

<sup>35</sup> This works as a normalisation, and can only be factored out if we work with linear perturbation theory. For any higher order, the initial perturbations must be including before evolving the system in time.

### 5.1.1. Physical observables

In order to measure the CMB we measure the temperature fluctuations as function of direction on the sky. In order to connect theory to these observations, we consider the temperature perturbation from Eq. (65), which is what we measure in experiments, and realise that this may be expanded in spherical harmonics (now in real space):

$$\Theta^{\text{Obs}}(\mathbf{x}, \hat{\mathbf{p}}, t) = \sum_{l=1}^{\infty} \sum_{m=-l}^l a_{lm}(\mathbf{x}, t) Y_{lm}(\hat{\mathbf{p}}), \quad (112)$$

where the angular dependency is taken care of by the *spherical harmonic functions*:  $Y_{lm}(\hat{\mathbf{p}})$ . From orthogonality of spherical harmonics,<sup>36</sup> we may express the coefficients  $a_{lm}(\mathbf{x}, t)$  as:

$$a_{lm}(\mathbf{x}, t) = \int d\Omega_{\hat{\mathbf{p}}} Y_{lm}^*(\hat{\mathbf{p}}) \Theta^{\text{Obs}}(\mathbf{x}, \hat{\mathbf{p}}, t). \quad (113)$$

It is important to note that Eq. (112) allows us to divide the temperature perturbations into a set of weighted basis functions, these being the spherical harmonics. These functions are eigenfunctions of the Laplace operator on a sphere, and describe how a function varies with direction (on a sphere). The  $l$ -subscript indicates the scale on which these variations occur (these are inversely proportional). Thus, the interpretation of the  $a_{lm}$  coefficients is the amplitude of temperature fluctuations across different scales,  $l$ . Since inflation predicts initial perturbations like  $\Theta$  to be Gaussian random fields it follows that the  $a_{lm}$ -s are also Gaussian random fields with mean 0 and variance  $C_l$  which is given by:

$$\langle a_{lm} a_{l'm'}^* \rangle = \delta_{ll'} \delta_{mm'} C_l. \quad (114)$$

Because of the Gaussian nature of  $C_l$ , it contains all the statistical information about  $\Theta$ , and this is what we refer to as the *angular power spectrum* (or just power spectrum). Thus, when making observations of the CMB, the  $a_{lm}$ -s are measured and the corresponding power spectrum is constructed as Winther et al. (2023):

$$\hat{C}_l = \frac{1}{2l+1} \sum_{m=-l}^l |a_{lm}|^2, \quad (115)$$

where  $\hat{C}_l$  is an estimator of the full power spectrum  $C_l$ , based on one realisation of the initial Gaussian random field, namely the realisation that is our observable Universe. For each  $l$ , we have  $2l+1$   $m$  values from which we infer the estimate in Eq. (115). Since we only have one universe to make measurements in, the statistical uncertainties of  $\hat{C}_l$  is highly dependent on  $l$ , since for low  $l$  there are very few components to measure. This gives rise to an intrinsic uncertainty in  $C_l$  known as *cosmic variance* which is governed by Dodelson & Schmidt (2020):

$$\left( \frac{\Delta C_l}{C_l} \right) = \sqrt{\frac{2}{2l+1}} \quad (116)$$

<sup>36</sup> Orthogonality of spherical harmonics:

$$\int d\Omega_{\hat{\mathbf{p}}} Y_{lm}(\hat{\mathbf{p}}) Y_{l'm'}^*(\hat{\mathbf{p}}) = \delta_{ll'} \delta_{mm'}$$

### 5.1.2. Constructing the angular power spectrum

When constructing an equation for  $C_l$  we start from Eq. (113) and expand this in it Fourier series:

$$a_{lm} = \int d\Omega_{\hat{\mathbf{p}}} Y_{lm}^*(\hat{\mathbf{p}}) \int \frac{d^3\mathbf{k}}{(2\pi)^{3/2}} e^{i\mathbf{k}\cdot\mathbf{x}} \Theta^{\text{Obs}}(\mathbf{k}, \hat{\mathbf{p}}, t), \quad (117)$$

which we further expand into multipoles

$$a_{lm} = \int d\Omega_{\hat{\mathbf{p}}} Y_{lm}^*(\hat{\mathbf{p}}) \int \frac{d^3\mathbf{k}}{(2\pi)^{3/2}} e^{i\mathbf{k}\cdot\mathbf{x}} \sum_{l=1}^{\infty} (2l+1)(-i)^l \mathcal{P}_l(\mu) \Theta_l^{\text{Obs}}(\mathbf{k}, t), \quad (118)$$

where  $\mu = \hat{\mathbf{p}} \cdot \hat{\mathbf{k}}$ . Next, we multiply with the complex conjugate  $a_{lm}^*$  in order to obtain:

$$\begin{aligned} a_{l_1 m_1} a_{l_2 m_2}^* &= \sum_{l_1=1}^{\infty} \sum_{l_2=1}^{\infty} (2l_1+1)(2l_2+1)(-i)^{l_1-l_2} \\ &\times \int \frac{d^3\mathbf{k}_1}{(2\pi)^{3/2}} \int \frac{d^3\mathbf{k}_2}{(2\pi)^{3/2}} e^{i(\mathbf{k}_1-\mathbf{k}_2)\cdot\mathbf{x}} \\ &\times \int d\Omega_{\hat{\mathbf{p}}_1} \mathcal{P}_{l_1}(\mu_1) Y_{l_1 m_1}^*(\hat{\mathbf{p}}_1) \Theta_{l_1}^{\text{Obs}}(\mathbf{k}_1, t) \\ &\times \int d\Omega_{\hat{\mathbf{p}}_2} \mathcal{P}_{l_2}(\mu_2) Y_{l_2 m_2}(\hat{\mathbf{p}}_2) \Theta_{l_2}^{\text{Obs}}(\mathbf{k}_2, t), \end{aligned} \quad (119)$$

which is a rather undelicate expression. Thankfully, there are a number of ways to make this simpler. Firstly, we note that

$$\begin{aligned} \langle a_{l_1 m_1} a_{l_2 m_2}^* \rangle &\sim \langle \Theta_{l_1}^{\text{Obs}}(\mathbf{k}_1, t) \Theta_{l_2}^{\text{Obs}}(\mathbf{k}_2, t) \rangle \\ &= \Theta_{l_1}(k_1, t) \Theta_{l_2}(k_2, t) \langle \mathcal{R}(\mathbf{k}_1) \mathcal{R}(\mathbf{k}_2) \rangle, \end{aligned} \quad (120)$$

where it follows from our Fourier normalisation convention that  $\langle \mathcal{R}(\mathbf{k}_1) \mathcal{R}(\mathbf{k}_2) \rangle = \delta^{(3)}(\mathbf{k}_1 - \mathbf{k}_2) P_{\text{prim}}(k)$ , where  $P_{\text{prim}}(k)$  is the *primordial power spectrum*. This delta function will simplify the  $k$ -integrals by demanding  $\mathbf{k} = \mathbf{k}_1 = \mathbf{k}_2$ .

Further, there is a very useful identity of spherical harmonics, which read Dodelson & Schmidt (2020):

$$\int d\Omega_{\hat{\mathbf{p}}} Y_{l_2 m_2}^*(\hat{\mathbf{p}}) \mathcal{P}_{l_1}(\mu_1) = \delta_{l_1 l_2} \frac{4\pi}{2l_1+1} Y_{l_1 m_1}^*(\hat{\mathbf{k}}). \quad (121)$$

From Eq. (121) we pick up a factor  $\delta_{l_1 l_2}$ , which will remove the two infinite sums in Eq. (119). We also rewrite the differential  $d^3\mathbf{k} = k^2 dk d\Omega_{\hat{\mathbf{k}}}$ . Ultimately, averaging over all ensembles of Eq. (119) yield:

$$\begin{aligned} \langle a_{l_1 m_1} a_{l_2 m_2}^* \rangle &= \frac{(4\pi)^2}{(2\pi)^3} \delta_{l_1 l_2} \int k^2 dk \Theta_{l_1}(k, t) \Theta_{l_2}(k, t) \\ &\times \int d\Omega_{\hat{\mathbf{k}}} Y_{l_1 m_1}^*(\hat{\mathbf{k}}) Y_{l_2 m_2}(\hat{\mathbf{k}}) \times P_{\text{prim}}(k) \\ &= \frac{2}{\pi} \int k^2 dk |\Theta_l(k, t)|^2 P_{\text{prim}}(k) \delta_{l_1 l_2} \delta_{m_1 m_2}, \end{aligned} \quad (122)$$

where we used orthogonality of the spherical harmonic in the last step. Comparing this to Eq. (114) yield the desired equation for the angular power spectrum:

$$C_l = \frac{2}{\pi} \int k^2 P_{\text{prim}}(k) |\Theta_l(k)|^2 dk, \quad (123)$$

where we have made it implicit that we evaluate today:  $\Theta_l(k) = \Theta_l(k, t_0)$ . In order to simplify this even more we take into account

that most inflationary models predict the primordial power spectrum to be of the form Dodelson & Schmidt (2020):<sup>37</sup>

$$P_{\text{prim}}(k) = \frac{2\pi^2}{k^3} A_s \left( \frac{k}{k_{\text{pivot}}} \right)^{n_s-1}, \quad (124)$$

which is characterised by its amplitude  $A_s$  and spectral index  $n_s$ . Armed with this, the power spectrum then becomes:

$$C_l = 4\pi \int_0^{\infty} A_s \left( \frac{k}{k_{\text{pivot}}} \right)^{n_s-1} |\Theta_l|^2 \frac{dk}{k}, \quad (125)$$

where we now integrate across the logarithm of  $k$ . It is worth noting that the quantity found theoretically from Eq. (125) is fundamentally different from the power spectrum we measure and construct using Eq. (115). This is because when evaluating Eq. (122) we average across the whole ensemble of possible realisations of the primordial Gaussian random field. Thus, the quantity we arrive at theoretically is the *ensemble averaged power spectrum*, while we are only able to observe the power spectrum for the one realisation that is our universe. However, when observing for large  $l$ -s we average across a large number of modes, which according to the *ergodic assumption* will be the same as the ensemble average Winther et al. (2023). Thus, we are able to accurately estimate  $C_l$  for sufficiently large  $l$ -s, but should run into cosmic variance for small  $l$ -s.

On last point to consider is that for a scale-invariant spectrum ( $n_s = 1$ ), the contributions from the Sachs-Wolfe terms yields (Dodelson & Schmidt 2020, Eq. 9.80):

$$l(l+1)C_l^{\text{SW}} = \frac{8}{25} A_s, \quad (126)$$

which is constants. Thus, it is conventional to consider the quantity  $\sim l(l+1)C_l$  and consider any deviations away from a constant horizontal line.

### 5.1.3. Matter power spectrum

The matter power spectrum describes the distribution of fluctuations in the matter density field in terms of scale. Evaluating it today yields information about the matter density at different physical scales, as we observe it today. It is given as Winther et al. (2023):

$$P(k, x) = |\Delta_{\text{M}}(k, x)|^2 P_{\text{Prim}}(k), \quad (127)$$

where  $\Delta_{\text{M}}(k, x)$  is known as the *growth factor* or *matter overdensity field*, and describe how the fluctuations in the matter density have evolved from some initial state until today. This initial state is again given by the primordial power spectrum,  $P_{\text{prim}}(k)$  as defined in Eq. (124), while  $\Delta_{\text{M}}(k, x)$  is given as:

$$\Delta_{\text{M}}(k, x) = \frac{2c^2 k^2 \Phi(k, x)}{3\Omega_{\text{M}} \mathcal{H}^2}. \quad (128)$$

We further define  $k_{\text{eq}}$  as:

$$k_{\text{eq}} = \frac{\mathcal{H}(x_{\text{eq}})}{c}, \quad (129)$$

which is the equality scale, evaluated at  $x_{\text{eq}}$  which is the time of matter-radiation equality. This scale corresponds to the wavenumber that entered the horizon at this time.

<sup>37</sup> In the special case that  $n_s = 1$ , the primordial power spectrum is called a *Harrison-Zel'dovich* power spectrum.

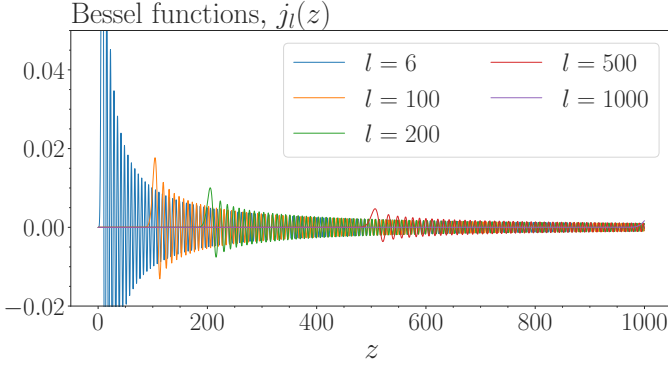


**Fig. 22.** The spherical Bessel function for selected  $l$ -values.

## 5.2. Methods

First things first, we are going to calculate a lot of spherical Bessel functions, since we need to integrate these across  $x$  in finding the transfer function (for every  $k$ ). Hence, it is computationally wise to spline them in advance. Further, we need to calculate the line of sight integral across all the  $x$ -values in order to obtain the transfer function. We may choose to compute the transfer function directly when integrating the power spectrum, or we may precompute it and then spline the result. We will choose the latter. Lastly, we integrate and compute  $C_l$  as functions of  $l$ . We expect this to be a relatively smooth function, so we choose a small finite number of  $l$ -s for which we perform the integral. The  $l$ -s we are going to use are the following:

$l \in [2, 3, 4, 5, 6, 7, 8, 10, 12, 15, 20, 25, 30, 40, 50, 60, 70, 80, 90, 100, 120, 140, 160, 180, 200, 225, 250, 275, 300 \dots 2000]$ , where the dots represent increments of 50.

### 5.2.1. Making Bessel splines

We may precompute and spline the spherical Bessel function since we know the minimal and maximum value of its argument. We need to compute for values of the argument  $z \equiv k(\eta_0 - \eta(x))$  where  $\eta_0$  is the current value. From Fig. 5 we have that  $\eta(x) \leq \eta_0$  for  $x \leq 0$ ,<sup>38</sup> so it becomes apparent that we need to precompute values for  $z \in [0, \eta_0 k_{\max}]$  for every  $l$ . Since the spherical Bessel functions oscillate with a period of approximately  $2\pi$ , we need to take enough samples in order to account for all effects. If we want  $n$  samples per oscillation we need to sample with a rate:

$$\Delta z = \frac{2\pi}{n_{\text{bessel}}}. \quad (130)$$

We will use  $n_{\text{bessel}} = 25$  and the result may be seen in Fig. 22, from which we clearly see that we sample with enough accuracy. The first peaks occur at around the value of the order of the function. One ending note is that if the argument  $z$  of the spherical Bessel functions are too large, some functions for finding it may break down, so proceed with caution.

### 5.2.2. Line of sight integration

We are now ready to perform the actual line of sight integration from Eq. (101). We are supposed to integrate from  $-\infty$  until today, but by investigating the integrand we may simplify this. Fig. 23 shows the integrand for a selected number of  $l$ -s. From the

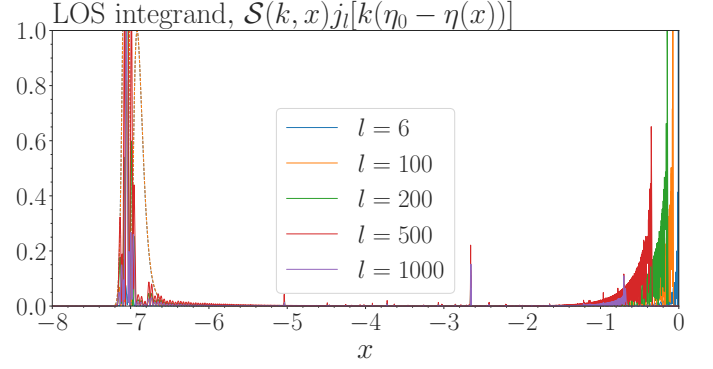


**Fig. 23.** Integrand of LOS integral, mostly governed by the source function. The contribution is very limited before, but peaked during recombination. We have some contribution between recombination and today due to the corrections to the source function. The plot shows (but indistinguishable) values for  $k = k_{\min}$  and  $k = k_{\max}$  in order to highlight the extreme effects.

discussion of the source function in Section 4.1.10, we would expect most of its contribution to be around the time of recombination. This is emphasized in the plot, and we also see some effects at later times, up until today. These are the correction effects to the source function, which we need to take into account. The take home message is that there is very limited contribution from the time before recombination, so we choose some time right before recombination from which we start the integration. According to Table 3, recombination happens at  $x \sim -7$ . If we then choose  $x = -8$  as our start of integration, we capture the effects we observe in Fig. 23. Further, before this time, both  $\bar{g}$  and  $e^{-\tau}$  is very close to zero, as can be seen from Fig. 13 and Fig. 12. This validates our choice of  $x = -8$ , which more than halves the points of  $x$  we need to integrate across, greatly improving computation time. We must also here pay close attention to the sampling of the integrand because of the oscillations, and because it is a function of both  $x$  and  $k$ . We sample w.r.t.  $x$  as follows:

$$\Delta x = \frac{2\pi}{n_{\text{LOS}}^{(x)}}, \quad (131)$$

and w.r.t.  $k$  as:

$$\eta_0 \Delta k = \frac{2\pi}{n_{\text{LOS}}^{(k)}}, \quad (132)$$

where we use  $n_{\text{LOS}}^{(x)} = 350$ , and  $n_{\text{LOS}}^{(k)} = 32$ , since the integrand is a lot smoother in  $k$  than  $x$ , we thus need a rather high resolution in  $x$ .

The result of the line of sight integral is the transfer function  $\Theta_l(k, \eta = \eta_0)$ , and can be seen for the same selected values of  $l$  in Fig. 24. It appears that our sampling was successful as we have captured the oscillations. This is by far the most time-consuming part of the integration, and the result is thus splined for easy access later on.

### 5.2.3. Integrate across $k$

When integrating across  $k$  in order to obtain the power spectrum  $C_l$  the main dependence on  $k$  is through the transfer function, so we use the same resolution as earlier for  $k$ . It is worth noting that integrating with respect to  $dk/k$  is equivalent to integrating with respect to  $d(\log k)$ , as long as we use the correct limits. It

<sup>38</sup> The line of sight integration is from early times until today, so we do not need to think about future value, hence  $x \leq 0$ .

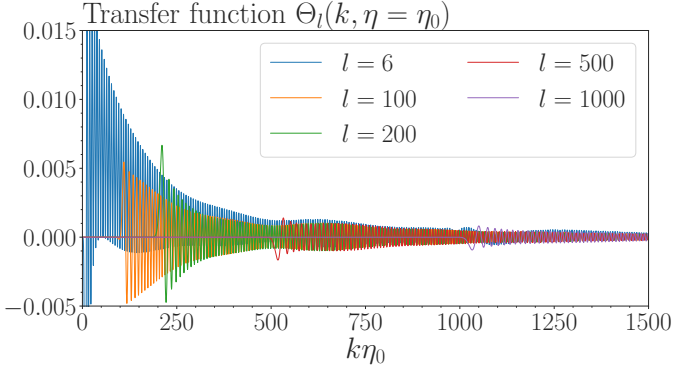


**Fig. 24.** Transfer function after performing line of sight integration for a selected number of  $l$ -s, as function of  $k$ .

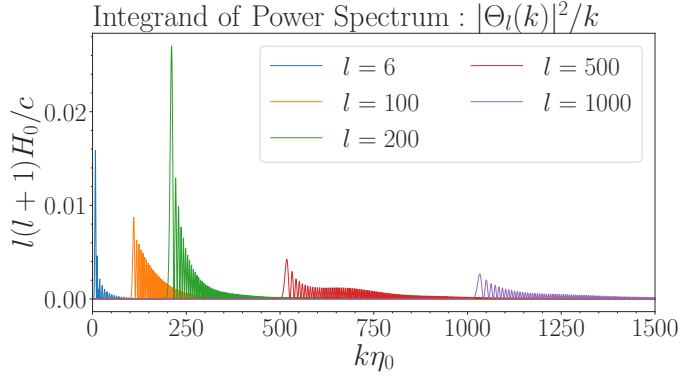


**Fig. 25.** Integrand of the power spectrum integral as function of  $k$ , given for a selected number of  $l$ -s.

is thus straightforward to compute the angular power spectrum in Eq. (125), and it is not very time-consuming since we have precomputed the transfer function already. Fig. 25 shows the integrand of the angular power spectrum integral, which is just the transfer function weighted by  $k$  (the primordial power spectrum is not included).

#### 5.2.4. Numerical integration

Due to the large sampling rate when the functions are not smooth, there is no point in wasting computational resources on a more accurate numerical integrator than the *trapezoidal method*. Since we specify samplings at constant spacing, we end up with a uniformly spaced domain, where we have  $N$  discretised spaces and  $N\Delta x = b - a$  where  $b$  is the maximum value of the domain and  $a$  the minimum. We approximate the finite integral as follows:

$$\int_a^b f(x)dx \approx \left[ \sum_{i=1}^{N-1} f(x_i) + \frac{f(x_a) + f(x_b)}{2} \right] \Delta x. \quad (133)$$

This method is used both when integrating across  $x$  and  $k$ .

### 5.3. Results and discussion

Fig. 26 shows the angular power spectrum as function of photon multipole  $l$ . The blue drawn line is the main power spectrum, while the dotted lines are the four constituents of the power spectrum that arise from the source function in Eq. (102). The red lines are observations taken from Aghanim et al. (2020), and the

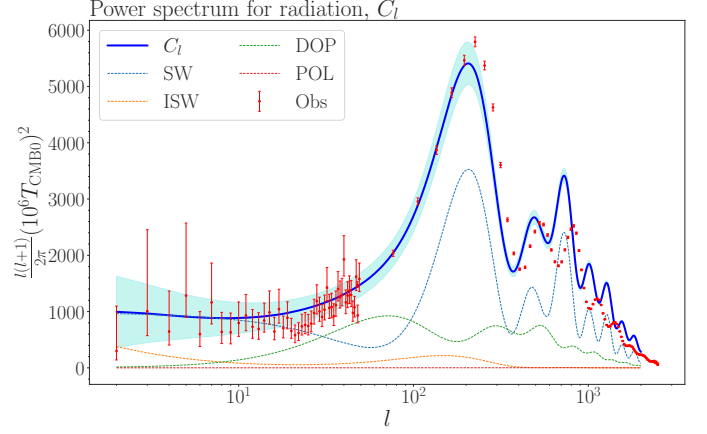


**Fig. 26.** Angular power spectrum as function of photon multipole  $l$ . The blue line shows the angular power spectrum itself with the intrinsic cosmic variance overplotted in turquoise. The dotted lines are the individual effect of the different constituents of the source function. The red error bars are observational constraints.

turquoise shade shows the theoretical cosmic variance as given in Eq. (116). As expected, since we ignore both polarisation and neutrinos there is a discrepancy between the observed values and the theoretical prediction. This is most prominent for larger  $l$ -s where the observational constraints are low due to high statistical accuracy. In discussing this results, we will focus on the three main parts of the plots, namely the *Sachs-Wolfe plateau* for low  $l$ -s, the *acoustic oscillations* for intermediate  $l$ -s and the *diffusion damping* for high  $l$ -s. Lastly we discuss the matter power spectrum in, where we have obtained the observational data from Chabanier et al. (2019) and Hlozek et al. (2012). It is worth noting the discrepancy between the data and prediction of the small scales. This could be a result of the various simplification we make, like ignoring neutrinos, polarisation and reionisation amongst other things.

#### 5.3.1. The Sachs-Wolfe plateau

The Sachs-Wolfe plateau is the part of the angular power spectrum that appear fairly flat for low  $l$ , i.e. large scales, hence its names. These large scales represent modes that had not yet entered the horizon at the time of recombination. According to the Sachs-Wolfe (SW) term in the source function in Eq. (102), the major contribution to the power spectrum are the temperature anisotropies present at the last scattering surface. This is the main contributor to the transfer function and thus the power spectrum itself. These effects are described by the photon monopole, and the value of the gravitational perturbation,  $\Psi$ , whose main effect slowed the photons down through gravitational redshift.<sup>39</sup> For large scales, that have not yet entered the horizon at the time of last scattering, the fluctuation to the gravitational perturbation have not yet been affected by causal physics. As a result, they closely resemble the initial perturbations induced by inflation.

The Sachs-Wolfe plateau may therefore be understood as a tracer of the primordial power spectrum. If we continue to assume this take the form of a primordial power spectrum parametrised by the amplitude  $A_s$  and spectral index  $n_s$  we are able to estimate the former by considering the amplitude of the Sachs-Wolfe plateau, and the latter by its shape.  $n_s = 1$  would

<sup>39</sup> Plus a small quadrupole correction.



generate a flat primordial power spectrum, whereas  $n_s > 1$  would give emphasis to small scales and vice versa.

We also take note of the large cosmic variance in this region. As already explained, this is an intrinsic feature of the angular power spectrum when comparing to observations, as we only have one universe to make observations in. The observational constraints are also significantly less accurate in this region, which is to be expected.

In figure Fig. 26 we also see some contribution from the integrated Sachs-Wolfe (ISW) term, which occur due to changes in the gravitational potentials. Most prominent in the discussion of the Sachs-Wolfe plateau is the late-time ISW which occur around matter-dark-energy equality. These effects can be seen for the largest scales, as they happened quite recently, and contributes to the minor deviations away from a straight line for the Sachs-Wolfe plateau.

There is also an increasing contribution of the Doppler term, which correspond to the peculiar velocity of matter (and our peculiar velocity relative to the CMB-frame). The Sachs-Wolfe plateau indicate the existence of large scale structures in the Universe, because of its power at the smallest  $l$ -s. It also provides valuable insight into the primordial power spectrum, and the process of inflation.

### 5.3.2. Acoustic oscillations

The acoustic oscillations seen at intermediate scales in Fig. 26 are a result of oscillations in the primordial plasma<sup>40</sup> in the very early universe. These oscillations are a result of primordial fluctuations in the dark matter distribution, effectively creating gravitational wells in which baryonic matter accumulate. In areas where the density of baryonic matter is increased, so is the photon pressure as well, due to their tight coupling. The gravitational wells thus have an attractive effect on the primordial plasma while the photon pressure have a repulsive effect. The interplay between these two effect source acoustic oscillations that travel throughout the universe.

The physics of gravitational attraction and radiative repulsion are both causal, so the effects from these phenomena may only be conveyed within causally connected regions. Thus, the scale for which these oscillations may be observed is closely governed by the causal horizon. Another thing to keep in mind is that this interplay between gravitational attraction and radiative repulsion require photons to be coupled to baryons. Therefore, we would think that the acoustic oscillations present at the last scattering surface is imprinted on the CMB and the angular power spectrum.

The first peak at around  $l \sim 200$  represent the first contraction of the plasma. This contraction and subsequent rarefaction creates oscillations in the primordial plasma, propagating with the speed of sound (found in Eq. (48)). The quantity measured in the angular power spectrum is the temperature fluctuations, not the oscillations themselves. However, the Sachs-Wolfe effect tells us that the radiation escaping from these oscillating fluctuations loses energy due to gravitational redshift. Anomalies in photon temperature are therefore tracers of the potential wells from which these oscillations occur. Since most photons we observe today have free-streamed to us from the surface of last scattering, the peaks and troughs of the angular power spectrum represents the different scales affected by these propagating oscillations at the time of last scattering. The first peak represents the largest of these scale, i.e. the scale corresponding to

the sound horizon at the time of last scattering. This is the mode that reached its first maximum value at the time of decoupling. In other words, it is the variation in photon temperature at this scale, due to the very first contraction of the primordial fluid.

The second and third peak subsequently correspond to the first rarefaction and the second compression. Smaller scales enter the horizon earlier in the radiation era, leaving more time between horizon entry and recombination. This means that smaller and smaller scales have been under the influence of causal physics for a longer time, being subjected to more and more compressions and rarefactions, but also diffusion (next paragraph). It is fair to assume that the imprint of each scale happens at slightly different times, since the *freeze-in* ultimately occur when the mean free path of photons becomes larger than the scale of the oscillating wave. However, in cosmic time these events are very close to each other, as the mean free path increased rapidly during recombination, so for all practical purposes we regard the freeze-in time to be the same across all scales. Similar arguments follow for the next peaks, but these are greatly affected by damping. It is also worth noting that the acoustic oscillations seen in Fig. 26 are mostly a result of the Sachs-Wolfe effect, i.e. the fluctuations of the gravitational potential at the time of last scattering. There is also a small contribution from the doppler term, due to the photon quadrupole. This effect ensures that the first peak is actually a peak and not a trough, as would be the case if we only considered the Sachs-Wolfe effect, which has a trough at around  $l \sim 60$ .

### 5.3.3. The damping tail

In the primordial plasma that existed before recombination, photons were tightly coupled to baryons (matter) via Thomson scattering. This resulted in an opaque environment, where photons had a short mean free path, and energy was interchanged with every collision. These interactions and consequent energy transfers caused the temperature fluctuations at small scales to be smoothed. In terms of angles, it is fair to assume that the scattering of photons off electrons causes a dispersion across all angles, as none should be favoured. All of this results in an averaging of the temperature in local neighbourhoods, effectively reducing the temperature fluctuations. The smaller the scale, the greater the effect. This phenomenon is called *silk damping* or more generally *diffusion damping*, Dodelson & Schmidt (2020). In Fig. 26 this can be observed as a damping tail towards the higher  $l$ -s, where the amplitude of the temperature fluctuations rapidly decrease, but still oscillating. The effect of the diffusion damping is thus to suppress the acoustic oscillations.

### 5.3.4. Parameter dependence

So far we have studied how the angular power spectrum actually appear with our choice of parameters, but how would this appearance change if we changed any of the free parameters? Let's start with the curvature parameter  $\Omega_{k0}$ : In our fiducial cosmology, the universe is almost completely flat. If however, we had an open universe ( $\Omega_{k0} > 0$ ), the entire power spectrum would have been shifted towards the right, i.e. towards smaller scales. From a geometrical point of view, an open universe is characterised by a hyperbolic conformal distance. This means that an angular separation measured today appears smaller than it actually is, emphasising the shift towards smaller scales for an open universe. Exactly the opposite argument may be used in order to explain why a closed universe, having parabolic conformal

<sup>40</sup> Plasma containing tightly coupled baryons and photons.



distance, would shift the spectrum towards larger scales. Similar effects would be seen if we changed the dark energy component, as this amounts to changing the acceleration of the expansion. A change in the acceleration rate changes how quickly the Universe cools down, and through this the time of recombination. Faster acceleration (more dark energy), cools the universe down faster, making recombination happen earlier, and the largest mode to freeze-in would correspond to a smaller scale, shifting the spectrum to the left. Similar argument, opposite conclusion for less dark energy.

Let's consider dark matter next. The amount of dark matter is the main contributor to the overall matter density, and thus driving the potentials. Increasing the dark matter content reduces the radiation driving effect, reducing the overall power of the peaks in the power spectrum. The amount of dark matter also affects the time of radiation matter equality, and since the Universe expands and cools at different rates in the different regimes this affect the time of recombination. More dark matter means the equality and also recombination happen at a later time. Therefore, we would see a small shift to the left (towards larger scales), as well as a reduction of the amplitude of the peaks if we increased the dark matter content.

In terms of baryonic matter, increasing it would make the compressions more powerful by accreting more matter per compression and deepen the well, increasing the baryon loading effect. This would in turn force the photons emitted to climb out from a deeper potential, increasing the power of the compressions. The radiative pressure will govern the rarefactions, and the gravitational blueshift of the photons. As a result, increasing the radiation pressure would increase the power of the rarefaction. Therefore, increasing baryonic matter would give more power to the odd peaks of the spectrum, whereas increasing radiation would give more power to the even peaks. Thus, the ratio between baryonic matter and radiation modulates the height of peaks, [Hu & Sugiyama \(1996\)](#).

### 5.3.5. The matter power spectrum

The matter power spectrum described in Eq. (127) is shown in Fig. 27. From Fig. 18 we see that during radiation domination, the cold dark matter perturbations grow logarithmically with the scale factor (linearly with  $x$ ), while the baryon perturbations oscillate with the photons. This is all for sub-horizon scales. The most dominant of the two is clearly the cold dark matter overdensity. What we draw from this is that the earlier a mode enters the horizon during radiation domination, the more suppression it undergoes from the logarithmic growth since the universe expands faster than the perturbation evolves, hence suppressing it.

After radiation matter equality, in the matter dominated regime the cold dark matter overdensity grow as a power law with the scale factor, faster than the expansion of the universe and increases. The baryon overdensity follows the cold dark matter after its decoupling from photons. Therefore, small modes entering the horizon before radiation matter equality are suppressed, while large modes entering the matter regime grow as a power of the scale factor. Modes entering later during matter domination would have less time to grow and would therefore be smaller. This is reflected in the matter power spectrum, which grows as  $P \propto k$  for large scales and  $P \propto k^{-3}$  for small scales, according to [Dodelson & Schmidt \(2020\)](#). The right side of Fig. 27 represents the small scale modes which entered the horizon during radiation domination. These fall off as  $k^{-3}$ . The smaller the mode, the earlier it enters and the more suppression it experiences. In this part of the spectrum we also see small

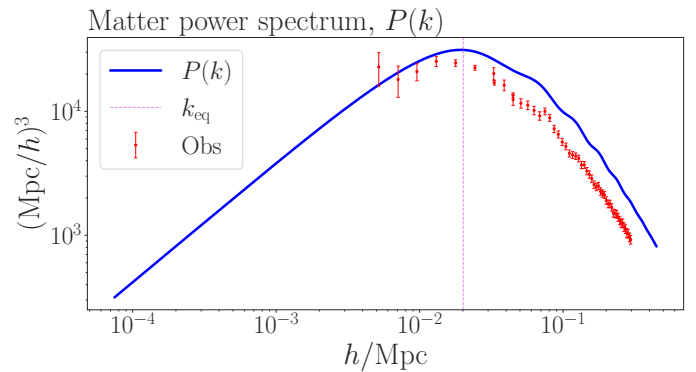


**Fig. 27.** Matter power spectrum as function of wavenumber  $k$ . The violet dotted line the equality scale, which is the wavenumber that correspond to the mode entering the horizon at the time of radiation-matter equality. The red error bars are observational constraints.

oscillations. These are the *baryon acoustic oscillations* (BAO), which originate in the coupling and joint oscillation of photons and baryons.

The left side of the figure represent the large scales, entering the horizon well into the matter dominated era, where the total matter perturbations evolve together as a power law w.r.t. the scale factor. Here the power spectrum go as  $k$ , where modes entering early (close to matter-radiation equality) have had the most time to grow. Altogether, this result in a peak in the matter power spectrum, marked as a violet line in the plot. This peak naturally occur at the radiation-matter equality, representing the scale which enters the horizon at this time.

Physically, the dark matter perturbation will just grow in space, while the baryon-photon overdensities will propagate as a wave outwards,<sup>41</sup> until recombination. At the time of recombination the photons decouple and we are left with an overdensity of baryons at a radius slightly larger than the sound horizon at decoupling. This is because the baryons will be dragged along with the photons for a short time after decoupling, since this does not happen instantaneously.<sup>42</sup> Eventually, dark matter will also start to cluster around this baryon overdensity, which emphasises it and creates what is analogous to a shell structure. This overdensity in the baryons is referred to as the BAO peak.

Linking this to the matter power spectrum: For large values of the power spectrum, there is a large variance of density, suggesting many over- and underdense regions. This suggests the presence of significant structures at these scales. For low values of the power spectrum, the variance decrease which means the presence of structures is smaller at these scales. So, there is a scale where we ought to expect *the largest amount of structure*, and that is the equality scale. In other words, the scale of the mode that enters the horizon at radiation-matter transition. The discrepancy between the observed values and the predictions for small scales is again due to the various simplifications we have done, here most notably ignoring neutrinos.

<sup>41</sup> From a single point, assuming this happens at every point in the Universe.

<sup>42</sup> There is also a drag effect due to neutrinos, but we have ignored neutrinos so far, so there is no point in including this now.

## 6. Conclusion

Throughout this project we have investigated the unperturbed FLRW background and its properties, the epoch of recombination, and perturbation to the FLRW background. All of this enabled us to construct the angular power spectrum of the CMB and the matter power spectrum for the total density contrast; quantities which we were able to compare with actual physical observables. These predictions were quite accurate for large scales, but showing a discrepancy larger than the observational uncertainties for the small scales. This is because we ignore the effect of neutrinos, polarisation and heavier elements when evolving the perturbation equations. We also do not consider the epoch of reionisation. Including all these effect would be a natural next step in improving our model. However, we are able to qualitatively discuss the physics behind most aspects of both power spectrums, having succeeded in our initial aim of producing a pipeline that numerically calculated the CMB power spectrum and matter power spectrum, given some cosmological model.

## References

- Aghanim, N., Akrami, Y., Ashdown, M., et al. 2020, *Astronomy & Astrophysics*, 641, A6
- Betoule, M., Kessler, R., Guy, J., et al. 2014, *Astronomy & Astrophysics*, 568, A22
- Callin, P. 2006, How to calculate the CMB spectrum
- Carroll, S. M. 2019, *Spacetime and Geometry: An Introduction to General Relativity* (Cambridge University Press)
- Chabanier, S., Millea, M., & Palanque-Delabrouille, N. 2019, *Monthly Notices of the Royal Astronomical Society*, 489, 2247
- Dodelson, S. & Schmidt, F. 2020, *Modern Cosmology* (Elsevier Science)
- Hlozek, R., Dunkley, J., Addison, G., et al. 2012, *The Astrophysical Journal*, 749, 90
- Hu, W. & Sugiyama, N. 1996, *The Astrophysical Journal*, 471, 542
- Ma, C.-P. & Bertschinger, E. 1995, *The Astrophysical Journal*, 455, 7
- Seljak, U. & Zaldarriaga, M. 1996, *The Astrophysical Journal*, 469, 437
- Weinberg, S. 2008, *Cosmology*, *Cosmology* (OUP Oxford)
- Winther, H. A., Eriksen, H. K., Elgaroy, O., Mota, D. F., & Ihle, H. 2023, *Cosmology II*, <https://cmb.wintherscoming.no/>, accessed on March 1, 2023